Design and fabrication of high-Q compact metal clad cavities coupled to InP waveguides

	InP Q
	2019-09-13
URL	http://hdl.handle.net/2261/00079325

Master's Thesis

修士論文

Design and fabrication of high-Q compact metal-clad cavities coupled to InP waveguides

（InP 導波路に結合した高 Q 値微小金属クラッド共振器の設計と作製）

37-175088
Yuguang Wang
王 宇光

Supervisor： Professor Yoshiaki Nakano

（指導教員：中野 義昭）

Department of Electrical Engineering and Information Systems
School of Engineering, the University of Tokyo

August　2019

Abstract

In order to meet the demands for ultra-compact and low-power devices for on-chip optical interconnect, various types of metal-clad cavity structures have been investigated, which offer distinctive advantages to achieve ultra-small device footprint, high thermal conductivity, and low-resistance electrical contact. However, since these metallic cavities are covered by metal, efficient light extraction and coupling to a waveguide has been one of the important issues.

In this research, I have introduced the detailed design and simulation result of the 2.3-μm-long metal-clad cavity integrated with an InP waveguide. Two essential parameters have been optimized through FDTD simulation. By optimizing the length of the cavity and thickness of the upper InP cladding, we maximized the Q factor of the resonant mode as well as the extinction ratio. We investigated that the extinction ratio could be enhanced significantly from 1.98 dB to 4.32 dB. Also, the Q factor enlarged from 296 to 535 in 2D FDTD simulation.

We also improve the fabrication process, especially the condition of HSQ and SiO_2 dry etching. From the transmission characterization, we successfully get the measurement of the resonance in the cavity at about 1500 nm, which agrees with the simulation result by FDTD.

To further enhance the Q factor at the resonance wavelength, we also numerically investigate a novel structure based on a horn-shaped metal-clad cavity, coupled to an InP waveguide. By adjusting the slope angle of the SiO_2 insulating layer, we demonstrated that the Q factor could be enhanced significantly from 152 to 408. We have then demonstrated the applicability of this structure to a compact modulator with an internal loss of 1.5 dB and the extinction ratio of 3.2 dB. We expect that the device performance could be further improved by optimizing the structure in the width dimension. The possibility of high-speed modulation is expected due to the low-resistance electrical contact of the metallic cavity. In the fabrication part, we successfully deposit the horn-shaped SiO_2 film by using the EB evaporator.

Contents

Chapter 1   Introduction

1.1   Optical interconnect

In recent years, due to the scale down of electronic device size, the performance of LSI has increased, but delays due to electric wiring and an increase in power consumption become problems. As means to solve this problem, optical interconnects: photonic integrated circuits are studied. It is thought to be able to demonstrate better performance without changing the carrier from electricity to light. In one way, the data load is multiplied by many orders compared with electric lines, which enables much more diverse and complicated applications. In another, the terminal devices are also becoming more miniaturized and mobile. [1-4]. Based on their advantages, this integrated optical device has been extensively studied in recent years. And as you can see from Fig. 1.1, the number of devices per chip increases exponentially from year to year.
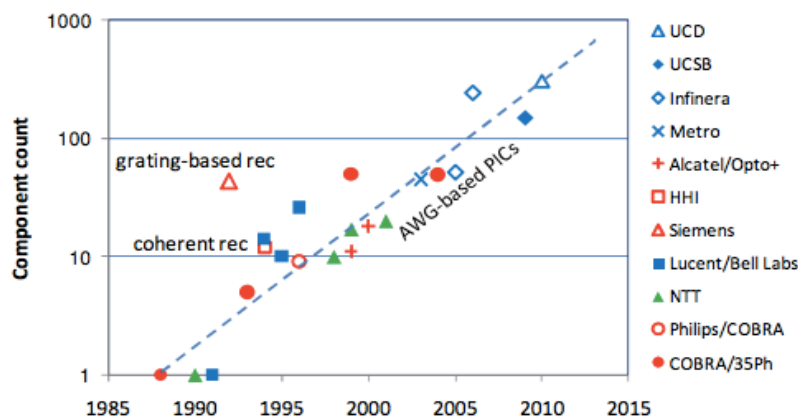
Fig. 1.1 Photonics Moore's Law of PICs [4]

As described above, data traffic has dramatically increased, but communication by electronic wiring between cores on a Si chip and copper wiring at server data centers is due to its power consumption and communication delay [5]. As wiring density and clock rate of silicon chip increase considerably, high energy consumption and propagation delay pose to be roadblocks for further development. This is also well-known as Interconnect Bottleneck:$E \geq CV^2$, where C is the capacitance of the wiring, and V is the voltage applied to the wiring. Since it is difficult to reduce the capacitance C, further energy saving is difficult when using electrical wiring. Also, the delay of

signal propagation is proportional to *RC,* where *R* is the resistance, so there is a limitation to low delay.

Fig. 1.2 Cross-section of hybridized interconnect structure [3]

Among them, the concept of photonic integrated circuit (PIC) was proposed by S. E. Miller in 1969 [6]. It is a device that integrates multiple photonic elements to achieve complicated. Many devices have been developed by research and development, such as optical switch elements and optical modulators. Concerning optical devices in PICs and optical interconnects, it is required to use nan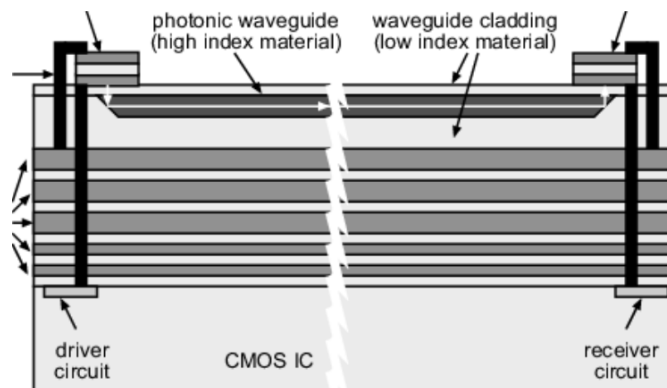oscale as a performance index, modulation speed of 10 *GHz* or more, energy consumption lower than 10 *fJ / bit* [7]. Nano cavities are attracting attention to meet these requirements.

1.2   History of nano devices

To meet the demands on small devices for optical interconnect, the metal-clad cavity has been greatly studied in recent years, which offers distinct advantages to achieve small device footprint, high thermal conductivity, and low-resistance electrical contact [8,9]. In addition to the improvement of their performance, miniaturization is also a remarkable trend. From Fig. 1.3, we can see the miniaturization of the laser by time.

In 1960, the first solid laser was made called Ruby Laser [10]. Moreover, the Semiconductor Laser was proposed two years later [11]. The vertical-cavity-surface-emitting laser (VCSL) was born in 1980, which shrank into 100 μm [12]. After that, a few micrometers size of microdisk laser demonstrated by using a 1300 nm wavelength InGaAsP/InP material for an active layer [13]. Although the dimension of laser is successfully shrunk over several micrometers, still larger than diffraction limit and light cannot be confined inside a volume which is smaller than its wavelength because of the intrinsic characteristic of electromagnetic waves.
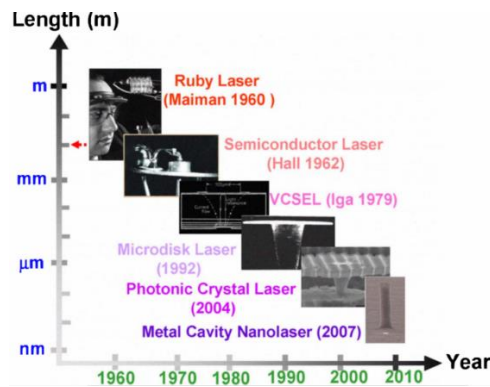
Fig. 1.3 The miniaturization of the nano devices by time [14]

Also, since 2007, when the metallic cavity semiconductor laser was demonstrated for the first time in the world broke the ice [14,15]. Fig. 1.4 (a) shows the structure of the metallic laser, which is mainly composed of three parts: semiconductor pillar, insulator thin film, and metal coating. The material of pillar from bottom to top is InP/InGaAs/InP/InGaAs, which forms a heterojunction. This structure enables lasing at near 1550 nm. The diameter of the pillar is about 260nm and the thickness of the active layer is 300 nm. Besides, insulators, such as SiN and SiO_2, can insulate the n and p region. The whole pillar is covered with gold. Light is confined inside the pillar, as shown in Figure 1.4(c). Since the skin depth of light is only 10s of nanometers, two metallic lasers can operate independently without any coupling even when they are very close to each other.

Fig. 1.4 (a) Structure of the cavity formed by a semiconductor pillar encapsulated in gold. (b) Scanning electron microscopy (SEM) image of a fabricated pillar without metal. The scale bar represents 103 nm. (c) Simulated electric-field intensity of the optical mode in the fabricated pillar [15].

3

1.2.1 Plasmonic devices
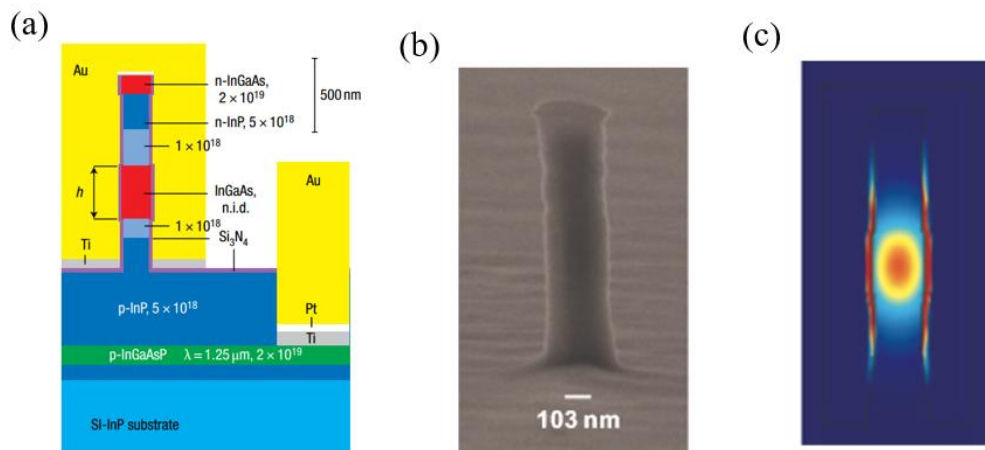
The metallic devices can be generally divided into two types: plasmonic devices and dielectric devices. A plasmonic laser is based on SPP (Surface Plasmon Polariton) that confines light beyond the diffraction limit ($\lambda_0/2n$) by using a state in which the vibration of an electromagnetic wave and the vibration of an electron on a metal surface are coupled [16]. The Plasmonic laser published in 2009 forms a MIM (Metal-Insulator-Metal) waveguide structure in which a thin semiconductor layer consisting of a heterojunction structure of InP and InGaAs is covered with Ag (Fig. 1.5) [17]. In the paper, a device with a semiconductor layer about 130 nm thick oscillates at an oscillation wavelength of 1470 nm at 78K. The threshold current is approximately 40 µA.
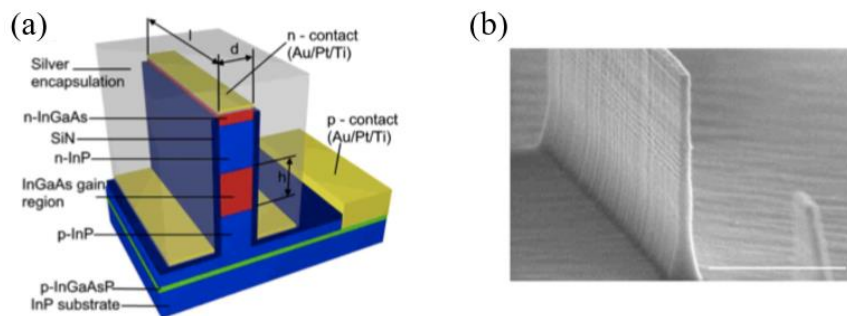
Fig. 1.5 (a) Structure of the MIM(Metal-Insulator-Metal) plasmonic laser. (b) SEM image of the semiconductor layer [16].

1.2.2 Dielectric devices

Dielectric device mainly uses metal clad as mirrors and plasmonic mode is unwanted. Fig. 1.6 shows the disk-shaped laser operating below 140K with a threshold current of 50 µA [18]. The metallic-dielectric cavity significantly enhances the quality factor ($Q > 1500$) of the wavelength and subwavelength scale lasers, and the pedestal structure significantly reduces the threshold gain ($< 400\ cm^{-1}$). This can potentially enable laser operation at room temperature.
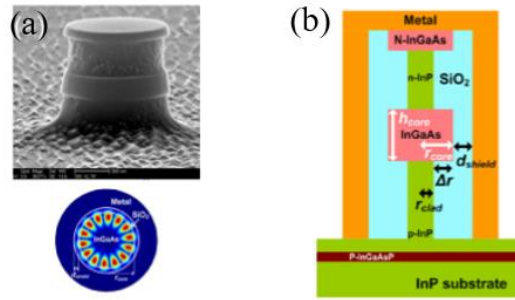
Fig. 1.6 (a) SEM image of the pillar and cross section │E│ profile. (b) Structure of the laser [18].

Another continuous wave sub-wavelength metallic cavity laser with electrical pumping was demonstrated in 2013 at room temperature [19,20]. The structure of the device is shown in Figure 1.7. A $1.15 \times 1.39 \times 1.7$ μm^3 rectangular laser with an (FP) Fabry-Perot like resonating mode in TM polarization. The threshold is 1.2 mA, not at μA, which is relatively large and current injection cannot exceed twice the threshold due to metal is lossy than expected at room temperature.
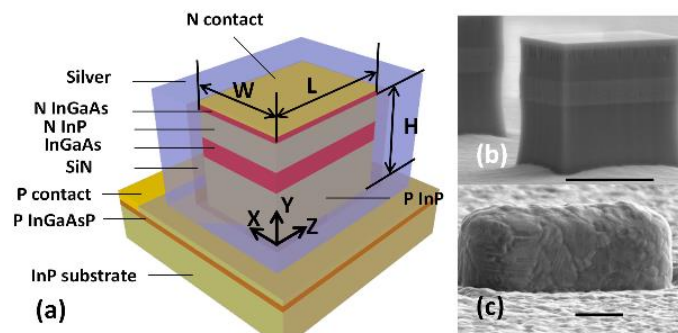
Fig. 1.7 Structure of sub-wavelength metallic cavity laser with electrical pumping [19].

From these examples above, we can find common difficulties for metallic cavity laser: low Q factor, difficult to extract and diffract (light extraction and diffraction become problems as it is emitted toward the substrate as shown on the left).

1.2.3   Metallic cavity coupled to the waveguide

By integrated with waveguide can solve these problems for its high coupling efficiency. By now, several coupling schemes have been proposed.
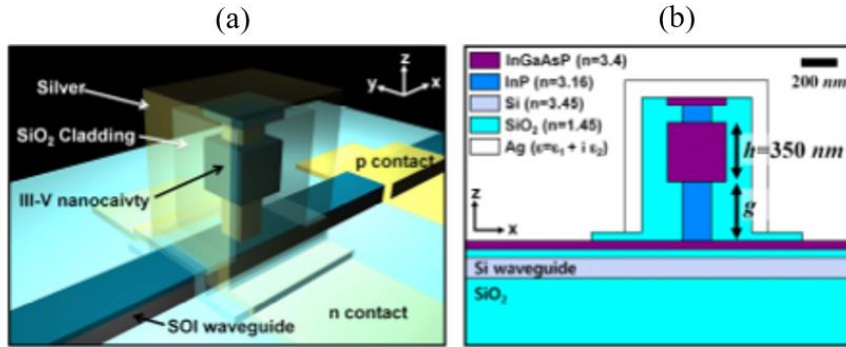
Fig. 1.8 Perspective (a) and cross-sectional (b) schematic views of a Si-waveguide coupled metal-clad nanolaser cavity. Here, the nanolaser cavity is designed as a cuboid structure with a height (h) of 350 nm, a width (w) of 350 nm, and a variable length (l) [21].

Fig. 1.8 shows the rectangular metal-clad nanolaser integrated onto a Si waveguide. The actual electromagnetic nanocavity consists of an InGaAsP bulk semiconductor cuboid with a height (h) of 350 nm, a width (w) of 350 nm, and a variable length (l) [21]. This design choses the SOI waveguide for its superior vertical confinement. Since many of the PIC devices are designed only for the fundamental mode, the single mode coupling is more preferred. In order to get a higher quality factor and external efficiency, further, optimize has been done by adjusting the insulator thickness. The emitted light is consumed in three ways: absorbed by the metal (γ_{metal}), coupled into the waveguide ($\gamma_{coupling}$) or emitted into the substrate ($\gamma_{substrate}$). By optimizing the insulator thickness, metal absorption (γ_{metal}) can be suppressed, but radiation ($\gamma_{coupling}+\gamma_{substrate}$) also increases. For result, it is found out that asymmetric thickness of the insulator can help lead the light into the waveguide so that 78% coupling efficiency $\gamma_{coupling}/(\gamma_{coupling}+\gamma_{substrate})$ can be achieved for a metal-clad nanolaser with a modal volume of 0.28 $(\frac{\lambda}{n})^3$ while maintaining a high optical quality factor of over 600. Finally, by engineering the bottom InP post height, the total external efficiency of the device can also be controlled efficiently. However, this structure is difficult to fabricate because the area needs to be changed between the core layer and the cladding layer, and the back surface must be thinned and coupled to the Si waveguide, so no example has been fabricated yet. Demonstration of the waveguide and metal resonator structure is required.

1.3   Research objective

In section 1-4, I have introduced some researches about small light emitters and confirm the metallic cavity semiconductor nano-laser to be a light source for on-chip optical interconnects. However, as mentioned before, the emitting light to the substrate brings extraction and diffraction problems and low Q factor. Coupling to waveguide can reduce the overall energy cost but difficult to demonstrate. So further investigation should be done to solve these problems.

1.3.1   Previous work in our laboratory

In our laboratory, we mainly focus on rectangular cavities for their better coupling to the waveguide. Moreover, we choose InP waveguide for coupling which can solve the fabrication problems. Fig. 1.9 shows the rectangular metallic cavity coupling into the InP waveguide [22]. By changing the thickness of D (Thickness of the upper InP cladding) can enhance both Q factor and coupling efficiency. As the simulation result of transmission, we can see there are two kinds of peak caused by two areas which occurred because of resonance with the different refractive index. Electric field distribution also shows the same result. Also, on the right is the result of the Q factor and extinction ratio of 2D and 3D simulation. Because of these two resonance modes, the result of 3D simulation shows low transmission and Q factor. And the resonance in the cavity failed to get in a measurement.
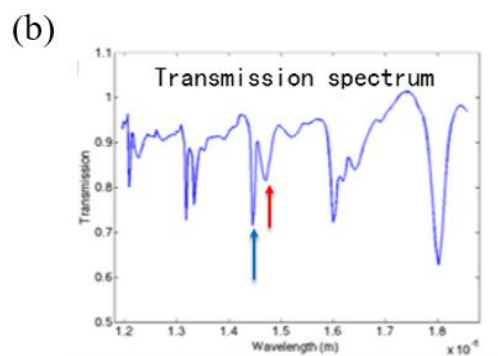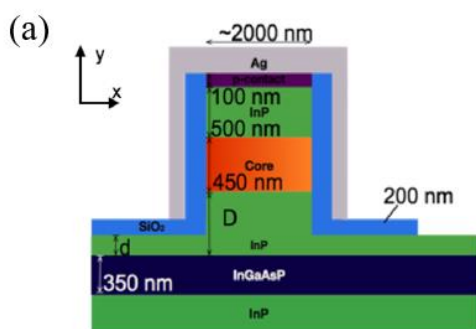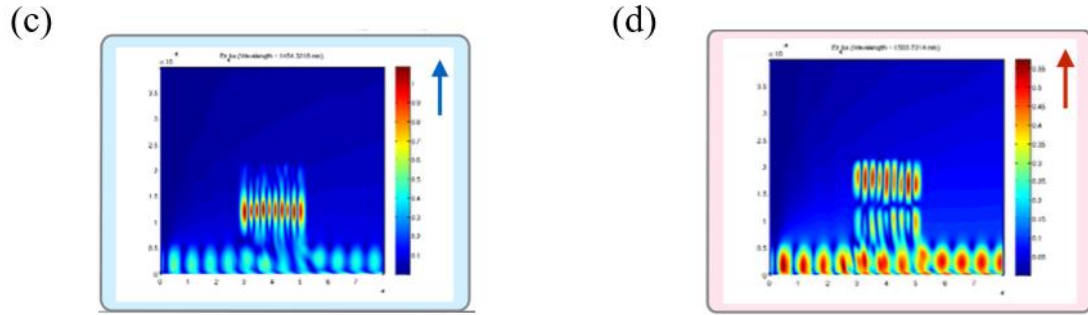
Fig. 1.9 (a) Schematic view of rectangular cavity coupled to InP waveguide. (b) Transmission spectrum of the structure. (c) and (d) electric field distribution of two kinds of peaks [22].

Although previous work has been done to make the metal-clad cavity coupling to InP waveguide, low Q factor and transmission cause the resonance in cavity failed to get in measurement. So new structure or further optimize of the cavity structure should be done to enhance the property of metal-clad cavity coupling to InP waveguide.

1.3.2   Purpose of this research

In this work, we aim to optimize the cavity structure to maximize the Q factor and minimize scattering loss by using a 2D-FDTD method. For further enhancement of Q factor, we numerically investigate a novel structure based on a horn-shaped metal-clad cavity, coupled to an InP waveguide. Recent work on the horn-shaped metal-clad cavity for on-chip light source application showed the possibility of reducing the plasmonic losses and improving the mode confinement by optimizing the slope angle [23,24]. We implement this concept to a small cavity integrated on an InP waveguide and optimize the structure to maximize the Q factor and minimize scattering loss. Then fabrication is attempted along with searching for better conditions. Finally, we carry out properties of the fabricated device. Analysis is also made between simulation and experimental results.

1.4   Structure of this thesis

This thesis is divided into 7 chapter:
In Chapter 1, the brief background of the metal-clad cavity is introduced.
In Chapter 2, brief principles involved in the metal-clad cavity are introduced
In Chapter 3, I will show the design and simulation results of metal-clad cavity, with comparison to previous ones.
In Chapter 4, I will explain the fabrication process and discuss important points in device fabrication.

In Chapter 5, I display the measurement results and evaluate the effectiveness of the design.

In Chapter 6, for further optimization, the design and simulation results of horn-shaped metal-clad cavity are introduced. Also the fabrication of the horn-shaped cavity will be discussed.

In Chapter 7, I will summarize all the work, and discuss the future improvement.

Chapter 2 Basic theory of metal-clad cavity

2.1 Basic principle of semiconductor laser

2.1.1 Double heterojunction

A double heterostructure is formed when two semiconductor materials are grown into a "sandwich." One material is used for the outer layers (or cladding), and another of the smaller band gap is used for the inner layer. The double heterostructure is a beneficial structure in optoelectronic devices and has interesting electronic properties. It makes the injected carrier tends to stay in the active layer and promote recombination, and it can confine light because it constitutes an optical waveguide.
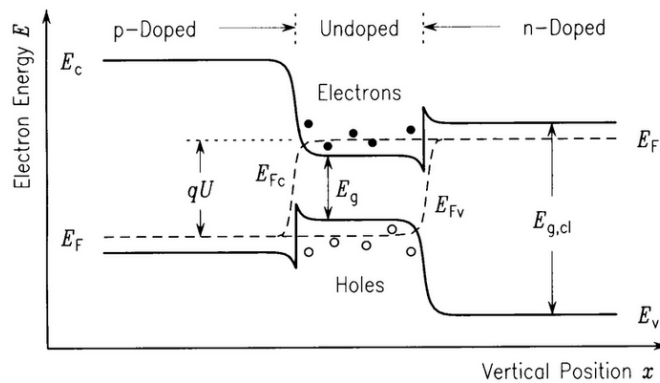
Fig. 2.1 Band diagram of forward biased double heterostructure [25].

As can be seen in Fig. 2.1, When a current is applied to the ends of the pin structure, electrons and holes are injected into the active layer from n-doped and p-doped region, respectively [25]. When electrons and holes meet together, they will have spontaneous emission (SPE). Once emitted, SPE photons are also available to stimulate other electron-hole pairs, so that stimulated emission (STE) is launched. Feedback is provided by cleavage plane or distributed Bragg reflector in convention lasers. Due to double heterojunction, carriers injected into the active region will be mostly confined and not able to jump over the barrier. Also, since substances with significant band gaps have small refractive indices, substances with different refractive indices are combined to form the optical waveguide structure described later. Therefore, light can be confined not only in the plane direction by the end face of the gain medium but also in the layer direction.

2.1.2   Lasing Mechanism

Fig. 2.2 (a) is structure of a typical commercial semiconductor cavity. Fig. 2.2 (b) shows Schematic of an active layer in a conventional Fabry-Pérot laser consists of two mirrors as optical cavity and gain medium inside the cavity. Semiconductor forms a strip waveguide, including a n active layer which can emit light when current injected. Emitted light travels in the waveguide back, reflecting at cleaved facets.
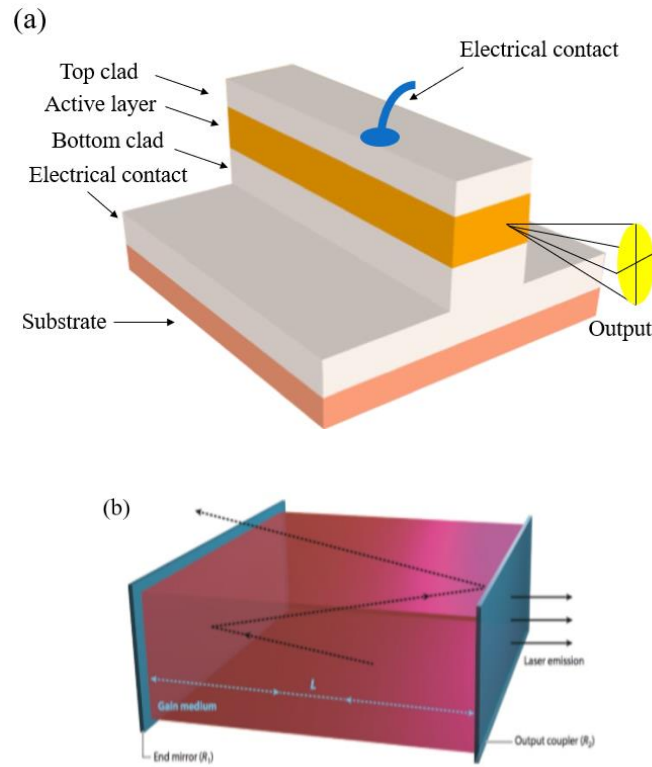
Fig. 2.2 (a) Schematic of typical commercial semiconductor cavity (b) Schematic of an active layer in a conventional Fabry-Pérot laser consists of two mirrors as optical cavity (length L) and gain medium inside the cavity [26].

Cleaved facet works as a mirror, whose reflectivity is around 0.3. Assume P_1 is optical power inside resonator, P_2 is optical power after one round-trip

$$P_2 = P_1 exp(-\alpha l)R_1 R_2 \tag{2-1}$$

The reflectivity of the two mirror surfaces are R_1 and R_2, respectively. l is length of resonator, and the loss factor of the gain medium $\alpha\ [cm^{-1}]$ Where α is average distributed loss if $\alpha > 0$, gain if $\alpha < 0$.

The loss is

$$exp\left(-2L\left[\alpha + \frac{1}{2L}ln\left(\frac{1}{R_1 R_2}\right)\right]\right) = exp\left(-2L\left[\alpha - \frac{ln\sqrt{R_1 R_2}}{L}\right]\right) \qquad (2\text{-}2)$$

We define

$$L \equiv gl + \alpha l - ln\sqrt{R_1 R_2} \qquad (2\text{-}3)$$

Where g is the gain. g can be regarded as absorption loss when $g > 0$, which is the usual case (when $g > 0$, it is a gain; when $g < 0$, it is a loss). Some special material for which g is minus when current injected can amplify the light and used in laser.
By calculating the Equation 2-1 to Equation 2-3, the power P_2 can be rewritten as

$$P_2 = P_1 exp(-2L) \qquad (2\text{-}4)$$

We set $P_2 = P_1$ because in a working laser, power remains the same. This time requires $L = 0$. So we can get

$$g = \frac{1}{l}ln\sqrt{R_1 R_2} - \alpha \equiv g_{th} \qquad (2\text{-}5)$$

Where g_{th} is threshold gain that compensate all the loss during light oscillation.

2.1.3   Rate equation

Laser diode is well described by focusing on carrier density N and photon density N_p by the rate equations.

$$\frac{dN}{dt} = \frac{n_i I}{qV_A} - \frac{N}{\tau} - R_{st} \qquad (2\text{-}6)$$

$$\frac{dN_p}{dt} = \Gamma R_{st} + \Gamma\beta_{sp}R_{sp} - \frac{N_p}{\tau_p} \qquad (2\text{-}7)$$

Where n_i is current injection efficiency; I is injected current; q is charge of one electron, V_A is volume of cavity, Γ is confinement factor, R_{sp} is spontaneous emission rate. R_{st} is stimulated emission rate which is related to the gain factor g mentioned above. β_{sp} is spontaneous emission factor representing the ratio of spontaneous emission that coupled into resonating mode. τ is lifetime of carrier and

τ_p is lifetime of photon in bulk. $\frac{N}{\tau}$ is total carrier combination rate, consisting of R_{sp} , R_{st} and non-radiative combination R_{nr}.

The R_{st} can be derived in Equation 2-6, where v_g is the group velocity and g is the gain per unit length.

$$R_{st} = v_g g(N)N_p \qquad (2\text{-}8)$$

As is known, the laser diode lasing when gain equals the loss,

$$\Gamma v_g g_{th} = \frac{1}{\tau_p} \qquad (2\text{-}9)$$

where g_{th} is the threshold gain. Combined with the relation: $\tau_p = Q/\omega$, we obtain

$$\Gamma Q = \frac{\omega}{v_g g_{th}} \qquad (2\text{-}10)$$

Where ω is the light angular frequency. ΓQ is the figure of merit for a laser and directly determines the required threshold gain g_{th}.

For a certain current I after lasing, stimulated photon density N_{st} can be obtained by combining Equation 2-9 and Equation 2-10:

$$N_{st} = \frac{n_i}{q v_g g_{th} V} (I - I_{th}) \qquad (2\text{-}11)$$

The output power is attributed by the radiative portion of photon density N_{st} which can be described by Equation 2-11.

$$P_{st} = \eta_d \frac{hv}{q} (I - I_{th}) \qquad (2\text{-}12)$$

The static characteristics of the laser can be analyzed by solving the time derivative component of the above rate equation as 0. By setting $\frac{dN}{dt} = 0$ and $\frac{dN_p}{dt} = 0$, we can get steady state of a working laser diode as well as dynamic response of laser diode by solving the equation numerically.

2.14 Q factor

Q factor is a dimensionless value that describes damping rate of resonator. It is defined as

$$Q = \frac{\omega P}{-dP/dt} \tag{2-13}$$

Where ω is angular frequency of light, P is stored energy in optical cavity, $-dP/dt$ is power dissipation rate. Solve the P from Equation 2-13, we can get

$$P(t) = P(0)exp(-\omega t/\, Q) \tag{2-14}$$

In the frequency domain,

$$Q = f_c\,/\Delta f \tag{2-15}$$

Where Δf is half width of spectrum of optical resonator, f_c is center wavelength of peak. High Q value leads to narrow half width. The larger Q value a resonator has, the stronger possible it can confine optical power within. On the contrary, Q value becomes smaller in the resonator where the loss of light is larger.

2.2 Analysis of metal-clad cavity coupling to waveguide

In this section, we describe the analysis method of the equivalent refractive index and the intensity distribution of the guided light for a basic symmetric three-layer slab waveguide.
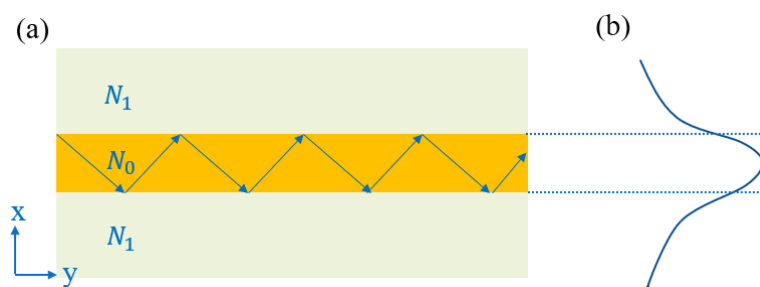

Fig. 2.3 Schematic of （a）TE mode light propagating in a symmetric three-layer slab waveguide, （b）E_y intensity distribution.

2.21   Three-layer slab waveguide

Fig. 2.3 (a) shows TE mode light propagating in the symmetric three-layer slab waveguide and its core layer. A material with a high refractive index is used as a core layer, and a material with a low refractive index which is used as a cladding layer, with the core layer sandwiched between. If the incident angle is larger than the critical angle at the interface between the core layer and the cladding layer, the light is totally reflected and confined in the core layer and travels through the waveguide. In the reflection at that interface, the phenomenon that light leaks into the cladding layer as an evanescent wave occurs, causing a phase change in the light. Another guiding condition is that the phase delay when reflected twice in the waveguide (after one round trip) is an integral multiple of 2π. Fig. 2.3 (b) shows the basic mode of $m = 0$. The conditional expression for this phase matching is shown in Equation 2-16

$$2m\pi = 2(k_0 N_0 cos\alpha \cdot W - 2\varphi) \tag{2-16}$$

Where $k_0 = 2\pi/\lambda$ and the propagation constant β is defined as

$$\beta \equiv k_0 N_0 sin\alpha \tag{2-17}$$

And the effective refractive index is

$$n_{eff} \equiv \frac{\beta}{k_0} = N_0 sin\alpha \tag{2-18}$$

The phase delay φ is expressed by the Equation 2-19 according to the Fresnel equation

$$tan\varphi = \frac{\sqrt{N_0^2 sin^2\alpha - N_1^2}}{N_0 cos\alpha} \tag{2-19}$$

To know the intensity of light in the waveguide, it is necessary to solve the wave equation. The Maxwell's equation is show below

$$\nabla \times E = -\frac{\partial B}{\partial t} \tag{2-20}$$

$$\nabla \times H = j + \frac{\partial D}{\partial t} \tag{2-21}$$

$$\nabla \cdot B = 0 \tag{2-22}$$

$$\nabla \cdot D = \rho \tag{2-23}$$

And we can rewrite the Maxwell's equation with angular frequency $\omega = e^{j\omega t}$,

$$\frac{\partial E_z}{\partial y} + j\beta E_y = -j\omega\mu_0 H_x \tag{2-24}$$

$$-\frac{\partial E_z}{\partial x} - j\beta E_x = -j\omega\mu_0 H_y \tag{2-25}$$

$$\frac{\partial E_y}{\partial x} - \frac{\partial E_x}{\partial y} = -j\omega\mu_0 H_z \tag{2-26}$$

$$\frac{\partial H_z}{\partial y} + j\beta H_y = j\omega\epsilon_0 n^2 E_x \tag{2-27}$$

$$-\frac{\partial H_z}{\partial x} - j\beta EH_x = -j\omega\epsilon_0 n^2 E_y \tag{2-28}$$

$$\frac{\partial H_y}{\partial x} - \frac{\partial H_x}{\partial y} = -j\omega\epsilon_0 n^2 E_z \tag{2-29}$$

Normally strip waveguide is used as oscillation cavity in semiconductor laser. Considering the TE mode only which propagates along z direction, Its Helmholtz equation can be written as

$$\frac{\partial^2 E_y}{\partial x^2} + \left(k_0{}^2 n^2 - \beta^2\right)E_y = 0 \tag{2-30}$$

$$-\frac{\beta}{\mu_0\omega}E_y = H_x \tag{2-31}$$

$$-\frac{1}{j\mu_0\omega}\frac{\partial E_y}{\partial x} = H_z \tag{2-32}$$

Where ω is angular frequency; n is refractive index and $n = \mathrm{n}_1$ $(-T < x < 0)$, $n = n_2$ $(x > 0\ or\ x < -T)$; $n = \sqrt{\varepsilon_r}$, ε_r is relative permittivity. We can solve the equation of E_y in three regions for a guided mode

$$E_y = Ce^{-qx}\ x \geq 0 \tag{2-33}$$

$$E_y = C(cos(hx) - \frac{q}{h}sin(hx))\quad 0 \geq x \geq -T \tag{2-34}$$

$$E_y = C(cos(hT) + \frac{q}{h}sin(ht))e^{p(x+T)}\quad x \leq -T \tag{2-35}$$

Where C is a normalization constant and h, q and p are given by

$$h = [(\frac{n_2\omega}{c})^2 - \beta^2]^{1/2} \tag{2-36}$$

$$q = [(\beta^2 - \frac{n_1\omega}{c})^2]^{1/2} \tag{2-37}$$

$$p = [(\beta^2 - \frac{n_3\omega}{c})^2]^{1/2} \tag{2-38}$$

These relationships are obtained from Equation 2-33 into 2-35.
The boundary conditions require that E_y be continuous at $x = 0$ and $x = -T$. The wavefunction in Equation 2-33 to 2-35 has been chosen such that E_y is continuous at both interfaces as well as $\frac{\partial E_y}{\partial x}$ at $x = 0$. By imposing the continuity requirements on $\frac{\partial E_y}{\partial x}$ at $x = -T$, we get

$$tan(ht) = \frac{p+q}{h(1-pq/h^2)} \tag{2-39}$$

This is the so-called mode condition. The propagation constant β of a TE mode must satisfy this condition. Given a set of refractive indices n_1, n_2 and n_3 of a slab waveguide, Equation 2-39 in general yields a finite number of solutions for β provided the thickness t is large enough. These modes are mutually orthogonal. The normalization constant C is again chosen so that the field represented by Equation 2-33 to 2-35 carries 1 W of power flow along the z axis in the mode. A mode of $E_y = AE_m(x)$ will thus correspond to a power flow of $|A|^2$W/m. The normalization condition is given by

$$-\frac{1}{2}\int_{-\infty}^{\infty} E_y H_x^* dx = \frac{\beta}{2\omega\mu}\int_{-\infty}^{\infty} E_m^2(x)dx = 1 \tag{2-40}$$

Where m denotes the m_{th} confined TE mode and $H_x = -i(\omega\mu)^{-1}\partial E_y/\partial z$. Substitution of Equation 2-39 for the wavefunction in Equation 2-40 and carrying out the integration lead to, after a few steps of algebraic manipulation,

$$C_m = 2h_m(\frac{\omega\mu}{|\beta|[t+(\frac{1}{q_m})+(\frac{1}{p_m})](h_m^2+q_m^2)})^{1/2} \tag{2-41}$$

The orthonormalization of the modes can be written as

$$\int_{-\infty}^{\infty} E_m E_1 dx = \frac{2\omega\mu}{|\beta|}\delta_{1,m} \tag{2-42}$$

Where $\delta_{1,m}$ is a Kronecker delta.

2.22 Metal-insulator-metal (MIM) waveguide

Electromagnetic waves couples with the oscillation of electrons at metal surface, energy of electromagnetic field exchanges with electronic energy. At the interface between metal and semiconductor, surface plasmon polariton (SPP) appears in which the collective vibration of free electrons on the metal surface and the electromagnetic wave are coupled [27，28]. This has the property of being localized at the interface between metal and semiconductor, so the MIM waveguide generates a mode distribution different from that of the semiconductor waveguide. Fig. 2.4 and 2.5 show the schematic and distribution of MIM waveguide.
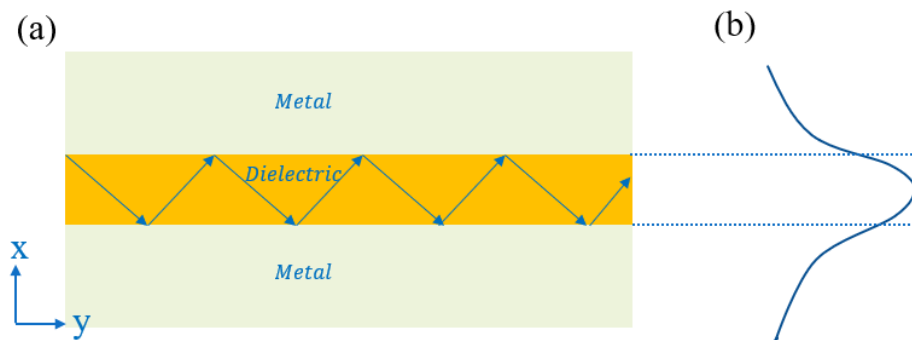

Fig. 2.4 Schematic of（a）metal-insulator-metal waveguide, dielectric is sandwiched between two metal layers.（b）Distribution of surface plasmon polaritons.
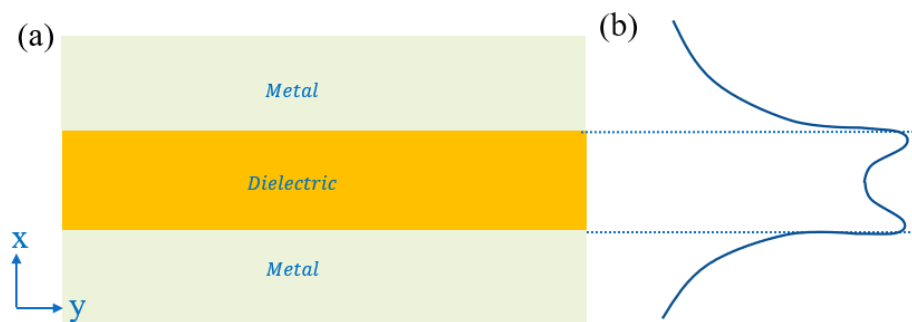

Fig. 2.5 Schematic of（a）metal-insulator-metal waveguide, dielectric is sandwiched between two metal layers.（b）Distribution of a dielectric mode.

Because TE polarized SPPs doesn't exist, we only consider TM mode in this waveguide. The Helmholtz equation of TM mode can be written as

$$\frac{\partial^2 H_x}{\partial y^2} + \left(k_0{}^2 - \beta^2\right)H_x = 0 \tag{2-43}$$

$$-\frac{\beta}{\epsilon_0 \omega n^2} H_x = E_y \tag{2-44}$$

$$\frac{1}{\omega \epsilon_0 n^2} \frac{\partial H_x}{\partial y} = E_z \tag{2-45}$$

Taking consideration of physics meaning, we can solve these equations for each area. The different point is that electrical field in core layer is located at $x = 0$ and $x = -T$, decaying exponentially. The solution for surface plasmon polaritons should be

$$H_y = -C\left(\frac{h}{q}\cos(hT) + \sin(hT)\right)e^{p(x+T)} \quad x \leq -T \tag{2-46}$$

$$H_y = C\left(-\frac{h}{q}\cos(hx) + \sin(hx)\right) \quad 0 \geq x \geq -T \tag{2-47}$$

$$H_y = -\frac{h}{q}Ce^{-qx} \quad x \geq 0 \tag{2-48}$$

Where C is a normalization constant and h, q and p are given by equation，and $\bar{q}$ as follows.

The continuity of H_y and E_z at the two interfaces leads, in a manner similar to the equation, to the eigenvalue equation

$$\tan(ht) = \frac{h(\bar{p}+\bar{q})}{(h^2 - \bar{p}\bar{q})} \tag{2-49}$$

Where

$$\bar{p} \equiv \frac{n_2^2}{n_3^2}p \quad \text{and} \quad \bar{q} \equiv \frac{n_2^2}{n_1^2}q \tag{2-50}$$

The normalization constant C is again chosen so that the field represented by Equation 2-49 and 2-50 carries 1W of power flow along the z axis per unit width in the y axis. We can get

$$\int_{-\infty}^{\infty} H_y E_x^* dx = \frac{\beta}{2\omega} \int_{-\infty}^{\infty} \frac{H_m^2(x)}{\varepsilon(x)} dx = 1 \tag{2-51}$$

Using Equation 2-51, we can get

$$C_m = 2\sqrt{\frac{\omega\varepsilon_0}{|\beta|t_{eff}}}\qquad(2\text{-}52)$$

And the effective waveguide width is

$$t_{eff} = \frac{\bar{q}^2+h^2}{\bar{q}^2}\left(\frac{t}{n_2^2} + \frac{q^2+h^2}{\bar{q}^2+h^2}\frac{1}{n_1^2 q} + \frac{p^2+h^2}{\bar{p}^2+h^2}\frac{1}{n_3^2 p}\right)\qquad(2\text{-}53)$$

2.3   Fabry-Perot etalon

The Fabry-Perot etalon, named after its inventors, can be considered as the best example of an optical resonator. It consists a plane-parallel plate of thickness l and refractive index n that is immersed in a medium of index n'. Generally, an etalon can be obtained by spacing two partially reflecting mirrors which apart the distance l, so that $n = n' = 1$. Another common form of etalon is produced by two-parallel faces on a transparent solid and then evaporating a metallic or dielectric layer on the surfaces.
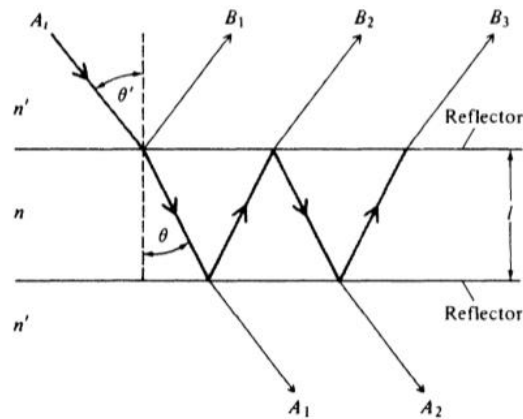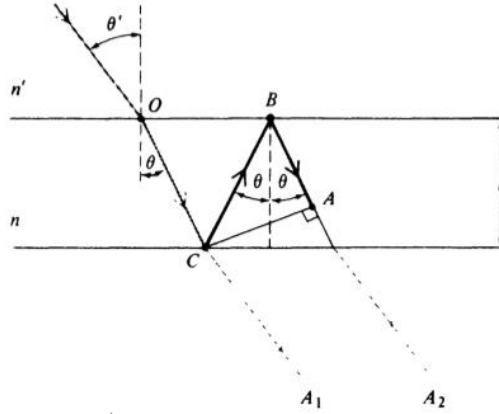

Fig. 2.6 The model of Fabry-Perot etalon [29]

Fig. 2.7 Path different between the reflection inside the of Fabry-Perot etalon [29].

As shown in Fig. 2.6, the plane wave incidents on the etalon at an angle θ' to the normal. The problem of transmission of the plane wave can be treated through the etalon by considering the infinite number of partial waves produced by multiple reflections at the two end surfaces. Fig. 2.7 shows the phase delay between two partial waves which is attributable to one additional round trip is given by

$$\delta = \frac{4\pi n l \cos\theta}{\lambda} = 2k_x l \qquad (2\text{-}54)$$

where λ is the vacuum wavelength of the incident wave, θ is the internal angle of the incidence, and k_x is the x component of the wavevector (x axis is perpendicular to the mirrors). At normal incidence, this phase shift is simply $\delta = 2kl$, where k is the wavenumber of propagation in the medium. Thus the phase shift is often called the round-trip phase shift.

If the incident intensity (watts per square meter) is taken as $A_i A_i^*$, we obtain following expression for the fraction of the incident intensity that is reflected by the etalon:

$$\frac{I_r}{I_i} = \frac{A_r A_r^*}{A_i A_i^*} = \frac{4R \sin^2\left(\frac{\delta}{2}\right)}{(1-R)^2 + 4R \sin^2\left(\frac{\delta}{2}\right)} \qquad (2\text{-}55)$$

Moreover, from

$$\frac{I_t}{I_i} = \frac{A_t A_t^*}{A_i A_i^*} = \frac{(1-R)^2}{(1-R)^2 + 4R \sin^2\left(\frac{\delta}{2}\right)} \qquad (2\text{-}56)$$

For the transmitted fraction. Our basic model contains no loss mechanisms, so conservation of energy requires that $I_t + I_r$ be equal to I_i, as is indeed the case.

21

For the transmission characteristics of a Fabry-Perot etalon. According to Equation 2-56 the transmission is unity whenever

$$\delta = \frac{4\pi n l cos\theta}{\lambda} = 2m\pi \qquad m = \text{any integer} \qquad (2\text{-}57)$$

The condition 2-57 for maximum transmission can be written

$$v_m = m\frac{c}{2nlcos\theta} \qquad m = \text{any integer} \qquad (2\text{-}58)$$

Where $c = v\lambda$ is the velocity of light in vacuum and v is the optical frequency.

2.4   Ring resonator

An optical ring resonator is a set of waveguides in which at least one is a closed loop coupled to some sort of light input and output. Under optical electronic devices can be designed to provide the possibility of switching or modulations. In free space, a ring resonator can be formed by using three mirrors oriented in a way beam of light can circulate along the triangle by three mirrors. Fig. 2.8 (a) shows the schematic of a ring resonator. We consider an input beam of amplitude A_i. At the first coupler, a fraction of the input beam will be propagating straight through, while a fraction of input beam will be coupled into ring. As the beam circulates inside the ring, multiple coupling occurs at the couplers. The simulation is similar to the case of multiple reflections in a Fabry-Perot etalon as shown in Fig. 2.8 (b).
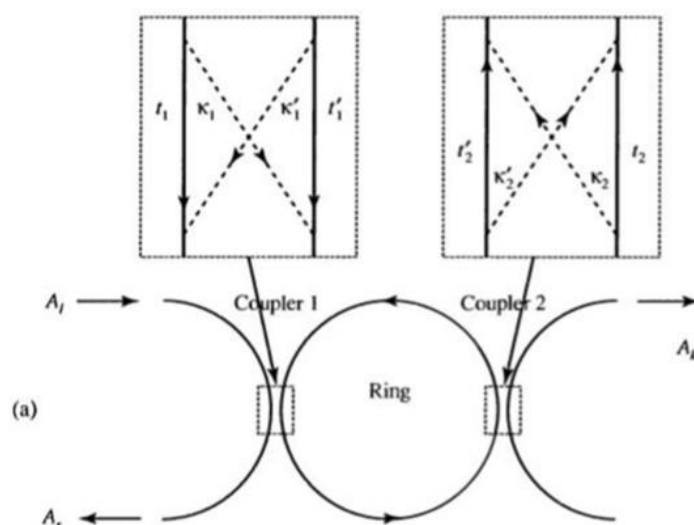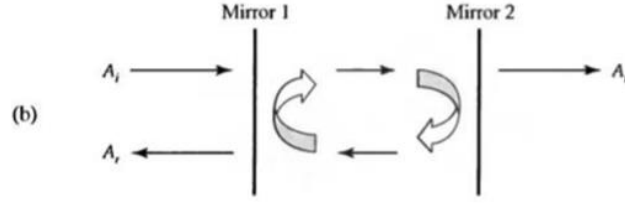
Fig. 2.8 (a) Schematic of the ring resonator and (b) The Fabry-Perot etalon with two mirrors [30]

The linear input-output relationship of the coupler can be written

$$\begin{bmatrix} B_1 \\ B_2 \end{bmatrix} = X \begin{bmatrix} A_1 \\ A_2 \end{bmatrix} = \begin{bmatrix} t & \kappa^* \\ \kappa & -t^* \end{bmatrix} \begin{bmatrix} A_1 \\ A_2 \end{bmatrix} \tag{2-59}$$

Where t is the straight-through coupling coefficient and κ is the cross-coupling coefficient. Note that the coupling matrix X is Hermitian($X = X^\dagger$), as a result of the choice of $|X| = -1$. These two coupling coefficients satisfy the following relationship.

$$|t|^2 + |\kappa|^2 = 1 \tag{2-60}$$

Matrix formulation can conveniently be employed to investigate the optical properties coupled resonators when several ring resonators are involved. The straight-through transmission coefficient of the ring resonator can be written

$$\sigma \equiv \frac{A_s}{A_i} = \frac{t_1 + t_2' a e^{-i\delta}}{1 - t_1' t_2' a e^{-i\delta}} = \frac{t_1 + t_2' a e^{-i\delta} e^{-\alpha d}}{1 - t_1' t_2' a e^{-i\delta} e^{-\alpha d}} \tag{2-61}$$

where $a = exp(-\alpha d)$, with α being an amplitude attenuation coefficient to account for loss due to bending or scattering. If we set $\kappa_2 = 0$ and $t_2 = -1$. This resonator is illustrated in fig. for this case, the straight-through transmission coefficient becomes

$$\sigma \equiv \frac{A_s}{A_i} = \frac{t_1 - a e^{-i\delta}}{1 + t_1' a e^{-i\delta}} = \frac{t - a e^{-i\delta}}{1 - t^* a e^{-i\delta}} \tag{2-62}$$

where δ is the phase shift inside the ring resonator, and $t_1' = -t_1^* \equiv -t^*$. By taking the absolute square of equation, we obtain the intensity transmission

$$|\sigma|^2 \equiv \left| \frac{A_s}{A_i} \right|^2 = \frac{a^2 - t^2 - 2atcos\delta}{1 + a^2 t^2 - 2atcos\delta} \tag{2-63}$$

Where, without loss of generality, by taking the t as a real number, the constant phase of t can always be lumped with the phase δ.

From this relation, as shown in Fig. 2.9, we can get two important features that are key for some potential applications. (1) The transmission $|\sigma|^2$ is zero at a value of coupling $a = t = \sqrt{1 - |\kappa|^2}$, known as the "critical coupling". (2) For high-finesse ring resonators with a low internal loss, the portion of the curve to the left of the critical coupling point is extremely steep. Small changes in a can control the transmission between zero and unity. We can also get high Q factor by controlling the transmission. Such a feature is desirable in the design of switching of modulation devices with a high modulation depth.
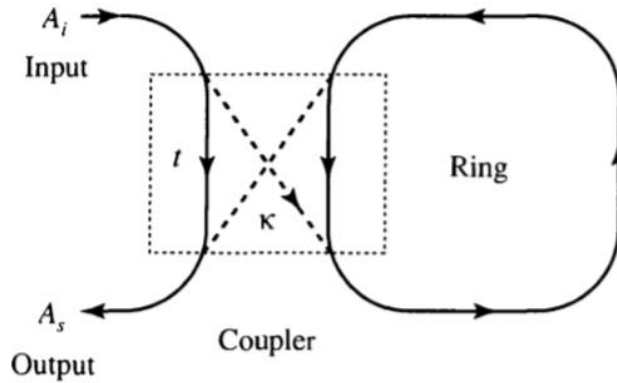

Fig. 2.9 Schematic of the ring resonator coupled with a waveguide, where t is the straight-through coupling coefficient and κ is the cross-coupling coefficient [30].

2.5   FDTD method

The FDTD (Finite Difference Time Domain) method is one of the numerical electromagnetic field analysis methods, and is a widely used analysis method at present. The FDTD method belongs in the general class of grid-based differential numerical modeling methods (finite difference methods). The time-dependent Maxwell's equations (in partial differential form) are discretized using central-difference approximations to the space and time partial derivatives. The resulting finite-difference equations are solved in either software or hardware in a leapfrog manner: the electric field vector components in a volume of space are solved at a given instant in time; then the magnetic field vector components in the same spatial volume are solved at the next instant in time; and the process is repeated over and over again until the desired transient or steady-state electromagnetic field behavior is fully evolved.

FDTD has turned out to be a very effective method to treat problems of electromagnetic wave which can be described by Maxwell's equations. The method discretizes both space and time to store values of electromagnetic components on every endpoint of the grid at evolving time points. In 1966, the presentation of Yee's lattice has made FDTD a highly robust way for computations of electromagnetic wave [31].
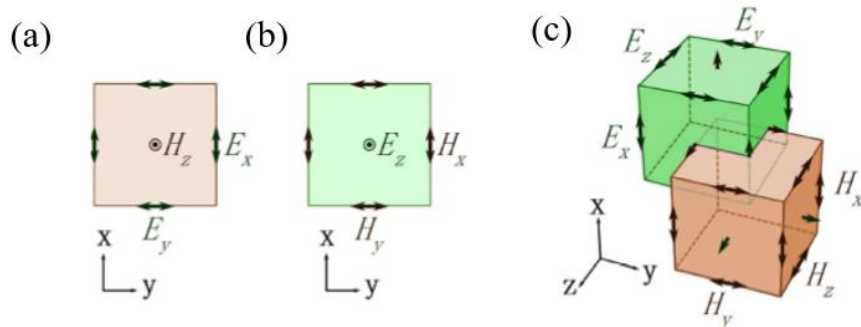

Fig. 2.10 Illustration of Yee's grid for FDTD. (a) and (b) are the 2D figures and (c) is the 3D figure [31].

As can be seen in Fig. 2.10 (c), electric component E and magnetic component H are staggered so that E value can be updated using surrounding H values and the E value of the previous time step and vice versa. Similarly, time is also staggered for electric and magnetic components. Iterations of the update result in a time-evolving process which indicates the development of the electromagnetic wave. Usually, 3D-FDTD calls for large memory and long calculation time. But the usually low Q factor for micro and nano optical devices make it possible to finish calculation in acceptable time durations.

Chapter 3 Design of metal-clad cavity coupled to InP waveguide

In previous work, the rectangular metal-clad cavity coupled to InP waveguide was proposed. However, the resonance in the cavity failed to get in measurement mainly due to the low transmission and Q factor. Thus, in this work, we aim to optimize the cavity structure to maximize the Q factor and minimize scattering loss by using a 2D-FDTD method. For further enhancement of Q factor, we propose the horn-shaped cavity structure, which can maximize the Q factor and minimize scattering loss. This will be investigated in Chapter 6.

This chapter will first explain the principle of the metal-clad cavity. Next, the digital design of the metal-clad cavity coupled to the InP waveguide will be introduced. The 2D-FDTD simulation results show the enhancement of Q factor and transmission. The calculation of the Q factor is also discussed, as well. Lastly, a brief summary is made.

3.1 Numerical design of metal-clad cavity coupled to InP waveguide

This time we implement this structure concept to a compact cavity integrated on an InP waveguide, and optimize the structure to maximize the transmission and minimize scattering loss. Fig. 3.1 shows the schematic of the horn-shaped metal-clad cavity considered in this work. The basic layer profile inside the metallic cavity is determined based on the results of our previous studies [37]; it consists of 450-nm-thick InGaAs (or InGaAsP) active layer sandwiched between the top and bottom InP claddings. The entire structure is capped with the SiO$_2$ insulation layer and thick Ag layer. Underneath the cavity, we insert a single-mode 350-nm-thick InGaAsP waveguide.
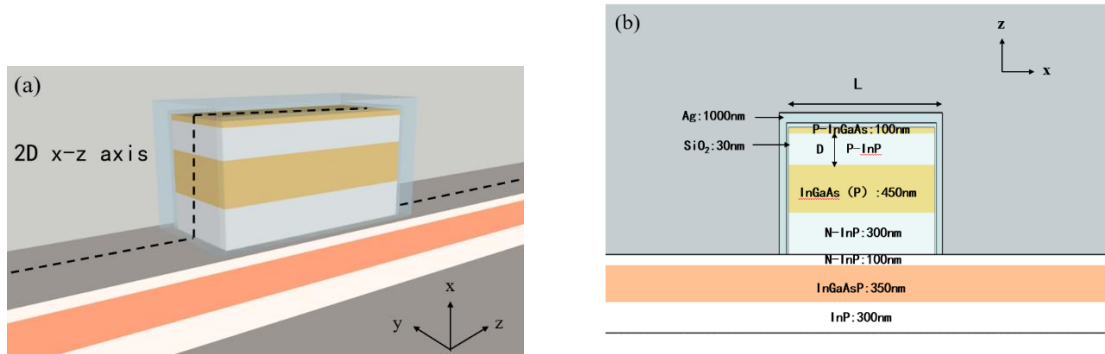

Fig. 3.1 (a) 3D Schematic and (b) the cross-sectional view at *x-z* plane of the metal-clad resonator.

By injecting current into the cavity, it could be used as a compact light source coupled to the InGaAsP waveguide [33-38]. Alternatively, it could also be used as a compact

photodetector by sending light through the InGaAsP waveguide and collecting the photocurrent generated inside the InGaAs active layer at the resonant wavelength. Finally, by applying reverse bias to modulate the refractive index and/or absorption of InGaAs or InGaAsP active layer, it could also be used as a resonant modulator. In this work, for convenience, we investigate this third possibility of using the structure as a compact modulator by sending the light from left side of the bottom InGaAsP waveguide and simulating the power transmitted to the right side of the waveguide in Fig. 3.1 (b).

Two important parameters that we aim to optimize are the length of the cavity L and the thickness of the upper InP cladding D. The device is analyzed by finite-difference time-domain (FDTD) method. The coupling mode of this waveguide coupled cavity is shown in Fig. 3.2.
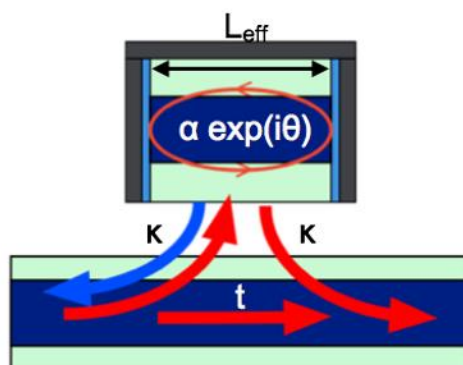

Fig. 3.2 Coupling mode of waveguide coupled cavity. Where t is the transmission coefficient, a is the internal loss and k is the coupling coefficient [22].

As talked in 2.22, the coupling mode of waveguide coupled cavity is similar with the ring resonator, and the transmission of the cavity can be calculated by

$$T^2 = \frac{a^2 - t^2 - 2atcos\delta}{1 + a^2t^2 - 2atcos\delta}$$ (3-1)

A TE fundamental mode is excited at the bottom InGaAsP waveguide, and the transmittance is obtained from the light transmitted through the cavity. The Q factor is derived from the damping rate of the electric field inside the cavity at the resonant wavelength. As the active InGaAs(P) layer in Fig. 3.1, we assume a bulk InGaAsP with the refractive index of 3.51 and negligible absorption to examine its applicability to a compact modulator.

3.2 FDTD simulation result

In this section, we will optimize the cavity structure using FDTD method. Since all two parameters have same effect at x-z direction as well as y direction, we will first optimize two parameters, L and D, through 2D FDTD simulation at x-z direction as shown in Fig. 3.1 (a). This part can save much simulation time because using 3D-FDTD will take much more time than 2D-FDTD.

3.2.1   2D-FDTD simulation (Optimize the length of cavity)

As shown in Fig. 3.2, both the length of cavity and the thickness of the upper InP cladding take great effect on transmission. So first we optimize the length of cavity while fixing D and α as $D = 200$ nm and $\alpha = 0$. Fig. 3.3 (a) shows the schematic image of optimizing cavity length.
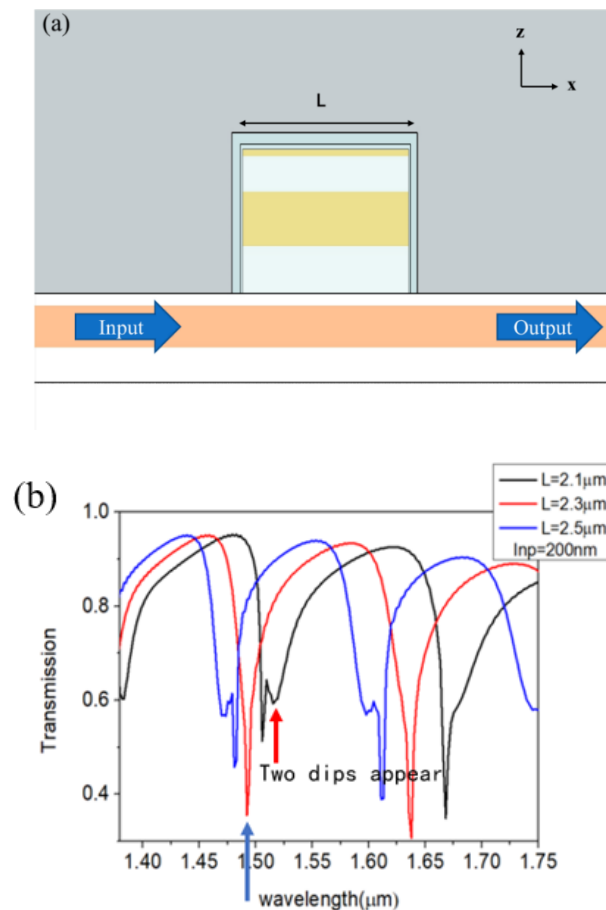

Fig. 3.3 (a) Schematic image and (b) Transmission spectrum for $L = 2.1\mu m$, 2.3 μm, and 2.5 μm ($D = 200$ nm, α = 0). Two dips emerge when $L = 2.1$ μm or 2.5 μm.

We sweep the L from 1.6 μm to 2.5 μm at InP thickness is 200 nm. To see it clearly, we show the transmission spectrum for $L = 2.1$μm, 2.3 μm, and 2.5 μm ($D = 200$ nm, $\alpha = 0$) in Fig. 3.3 (b). We can see two dips emerge when $L = 2.1$ μm or 2.5 μm. These dips (red arrow and blue arrow shown in Fig. 3.3 (b)) correspond to two resonant modes with different effective refractive indices. Two resonant modes will also drop down the Q factor in cavity and make it hard to measure the resonance mode. The electric field distributions also show the same result as we can see in Fig. 3.4. It is said that it occurs in the cavity core as the blue arrow in the figure, and in the InP clad in the cavity with the red arrow in Fig. 3.3 (b).
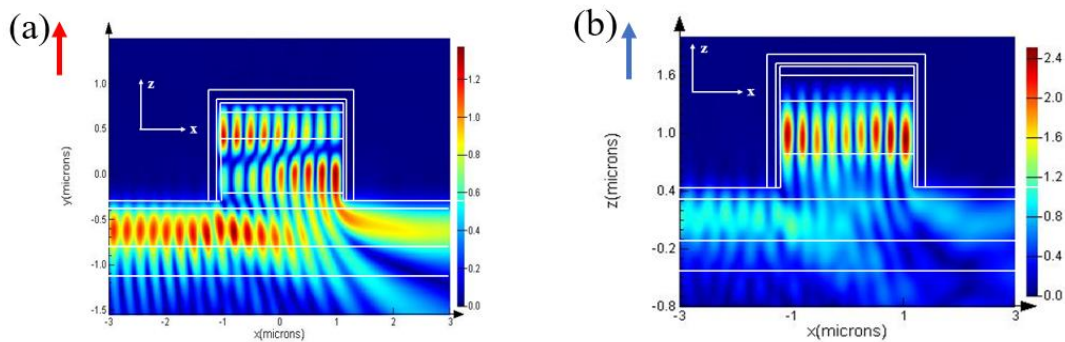

Fig. 3.4 (a) and (b) Electrical field distribution of two resonance mode show in Fig.3.5 (b). (a) shows the resonance mode in the InP clad in the cavity and (b) shows the resonance mode in the cavity core.

By adjusting L, they merge into one and the Q factor is maximized from 296 to 530 when L is 2.3 μm. Fig. 3.5 shows Q factor of resonant mode as a function of L.
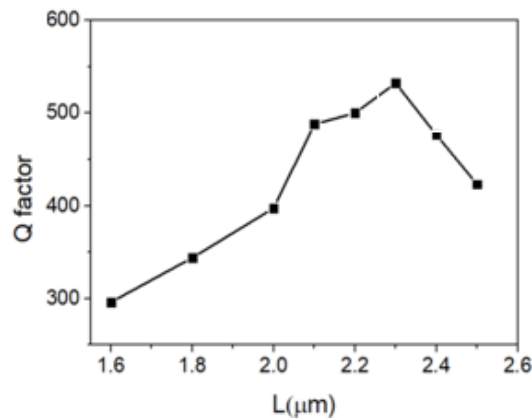

Fig. 3.5 Q factor of resonant mode as a function of L. The pick of Q factor get at L is 2.3 μm.

3.2.2 2D-FDTD simulation (Optimize the thickness of InP cladding)

Next part we optimize InP cladding thickness D for L = 2.3 μm and α = 0. Fig. 3.6 shows the Schematic image of optimizing the thickness of InP cladding. Fig. 3.7 (a) shows the simulated transmission spectrum for D = 100 nm, D = 300 nm, and D=500nm. Similar to Fig. 3.3, two dips converge when D = 300nm, where the Q factor is also maximized.
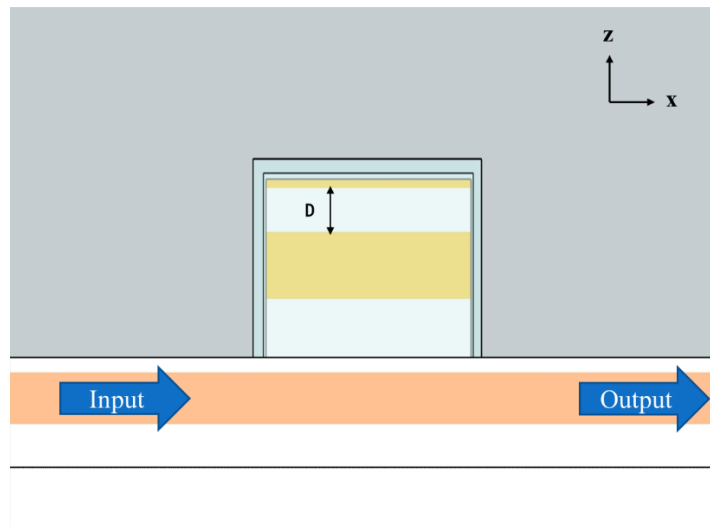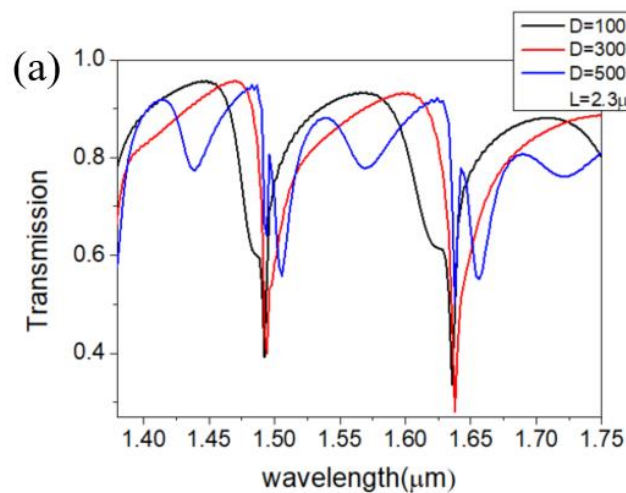

Fig. 3.6 Schematic image of optimizing the thickness of InP cladding

The Q factor increased because of two resonance mode merge into one. From the above results, we derive the optimized parameters as L = 2.3 μm and D = 300 nm. The Q factor in this case is 535.
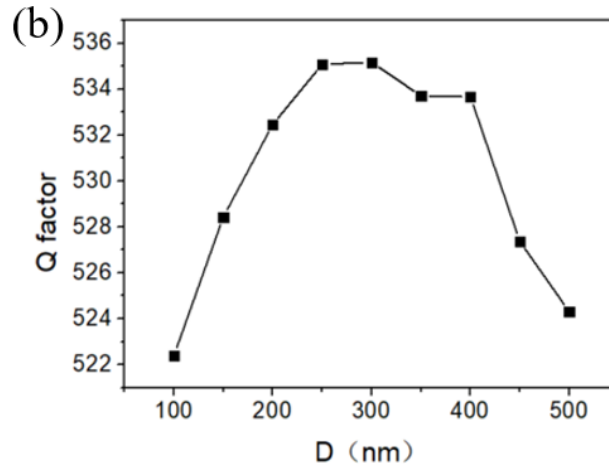
Fig. 3.7 (a) Transmission spectrum for $D = 100$ nm, 300 nm, and 500 nm ($L = 2.3$ μm, $\alpha = 0$). (b) Q factor of resonant mode as a function of D.

3.5 Summary

In this chapter, I have introduced the detailed design and simulation result of the 2.3-μm-long metal-clad cavity integrated with an InP waveguide. Two important parameters have been optimized through FDTD simulation. By optimizing the length of cavity and thickness of the upper InP cladding, we maximized the Q factor of the resonant mode as well as the extinction ratio. We investigated that the extinction ratio could be enhanced significantly from 1.98 dB to 4.32 dB. Also, the Q factor enlarged from 296 to 535 in 2D FDTD simulation.

Chapter 4　Fabrication of metal-clad cavity coupled to waveguide

4.1　Fabrication process flow

The layer structure of used wafer is shown in Table 4-1. The 350 nm thick InGaAsP layer is used as waveguide core which is expected to offer good confinement of light. The fabrication process flow of waveguide coupled metal-clad cavity is shown in Fig. 4.1. We first list the main steps used in the fabrication process below and describe them in detail in the next section.

Table 4-1 Layer structure of wafer

No.	Layer	Material	Thickness (nm)	Doping (cm^{-3})
1	P-contact	P-InGaAs	100	$> 1 \times 10^{-19}$
2	Upper clad	P-InP	480	5×10^{17}
3	Etch stop	U-InGaAsP	8	
4	Buffer	U-InP	20	
5	Active core	U-InGaAs	450	
6	Bottom clad	N-InP	400	5×10^{17}
7	Waveguide core	N-InGaAsP	350	5×10^{17}
8	Bottom clad	N-InP	200	5×10^{17}
9	Bottom clad	N-InP	250	5×10^{18}
10	Etch stop	N-InGaAsP	100	$>5 \times 10^{18}$
11	Buffer	N-InP	50	$>5 \times 10^{18}$
12	Substrate	N-InP		

Legend: InGaAs, SiO$_2$, Ag, InP, Cr, InGaAsP, HSQ

(a)   Wafer cleaning

(b)   SiO$_2$ deposition
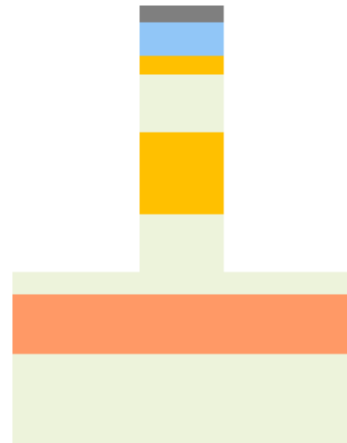
(c) Cr deposition

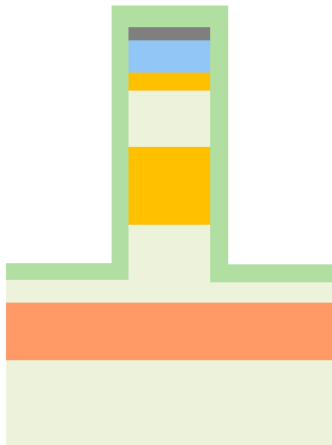(d) Spin coat HSQ resist
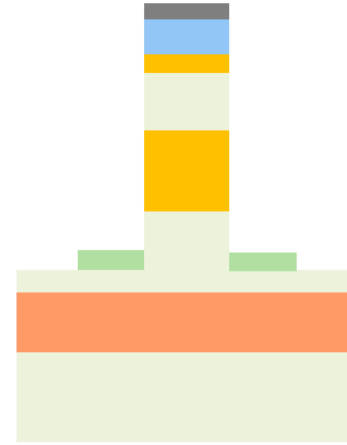
(e) EB exposing and develop

(f) Dry etch Cr
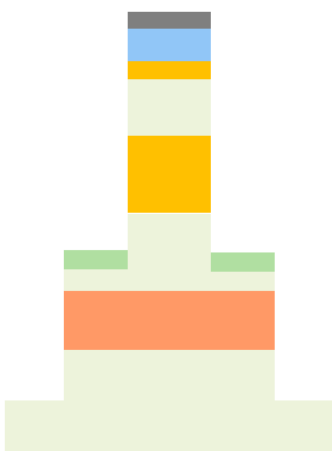
(g) Dry etch SiO$_2$
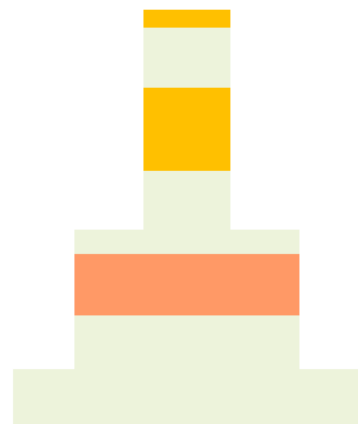
(h) Dry etch InP and InGaAsP to develop cavity

(i) Spin coat HSQ resist again

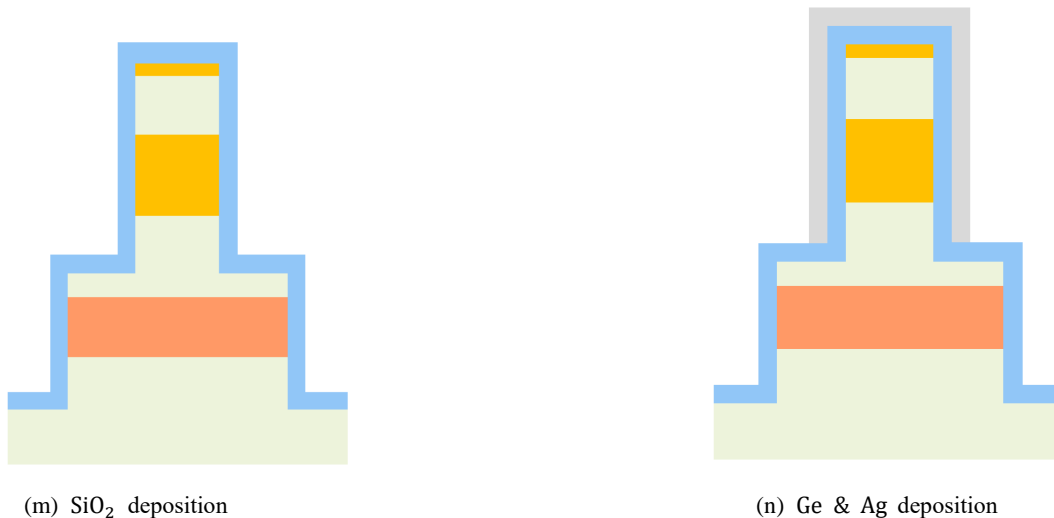(j) EB exposing and develop again

(k) Dry etch InP and InGaAsP to develop waveguide

(l) Remove hard mask and surface cleaning

(m) SiO_2 deposition

(n) Ge & Ag deposition

(a) Wafer cleaning. Wafer cleaning is made by acetone, isopropyl alcohol (IPA) and ethanol. We first dipped the wafer into acetone for 10 seconds, and then rinsed by (IPA) and ethanol for 1 minute, respectively. After that, put wafer on 200°C hotplate for 10 minutes to dissipate any liquid molecule remains on wafer.

(b) SiO_2 deposition. 400 nm thick SiO_2 as the hard mask during dry etching is deposited by plasma enhanced chemical vapor deposition (PECVD) during 350°C. It is said that SiO_2 deposited by PECVD is more robust than that formed by sputtering or vacuum evaporation, so that pattern degrades less during dry etching process. And thicker SiO_2 layer can meet our needs since we have to etch the InP more than 1.2 μm. Table 4-2 is the condition of SiO_2 deposition.

(c) Cr deposition. 30 nm thick Cr layer which can increase dry etching selectivity ratio is deposited on SiO_2. In our comparison experiment, the Cr layer either deposited by sputtering or vacuum evaporation shows similar robustness. This time we use vacuum evaporation to deposit for its high evacuation. Table 4-3 is the condition of Cr deposition by sputtering.

Table 4-2 Condition of SiO_2 deposition

Gas flow (sccm)	5% SiH_4/N_2O (170.0/710.0)
Chamber pressure (Pa)	134.0
RF power (W)	20
Temperature (°C)	350
Deposition rate	1 nm/s

Table 4-3 Condition of spin coating HSQ

	Step 1	Step 2 (for cavity EBL)	Step 2 (for waveguide EBL)
Rotation per minute(rpm)	500	3000	4000
Ramp-up time (second)	5	5	5
Holding time (sec)	5	60	60

(d) Spin coat HSQ resist. This time we use HSQ as the resist for EB lithography. Although HSQ is a negative resist, the side walls are said to be smoother in dry etching than other resists. So HSQ is a good choice for state-of-the-art fabrication [39]. It is reported that the sub 10 nm nano-wire patterning by HSQ has the good edge roughness [40]. Wafer is cut into 10 mm × 10 mm pieces for HSQ spin coat. Spin coat condition for HSQ is set as Table 4-4. 3 of 4 drops of HSQ resist are dripped onto center of sample immediately after rotation rate reach 500 rpm. It is worth noting that HSQ is very sensitive to operation condition. Any changes in the parameters and condition in Table 4-4 would cause unexpected affect in resist thickness and uniformity, which result in negative consequence during lithography [41]. After spin coating, HSQ is baked under $150°C$ for 2 minutes. The ideal thickness of HSQ should be 120 ~200 nm under spin coating condition.

(e) EB exposing. The EBL is done by F7000S-VD02 from Advantest company. Electron acceleration voltage is fixed to 50 kV. Dosage for 1 μm × 2 μm pattern is around 1800 $\mu C/cm^2$ for the cavity and 2000 $\mu C/cm^2$ for the waveguide. The drawing pattern used a general GDS file converted to the bef20 format by the conversion software BEAMER. In the bef20 format, GDS-defined patterns are converted to fill rectangular stamps of various sizes, enabling high-speed and fine-grained drawing.

Developing resist. After exposure, we use NaOH / NaCl / H_2O as developer with solution ratio of (1%:4%:95%) [41] [42]. we dipped the sample chip into it under room temperature for 25 to 40 seconds (which depends to the number of cavities on one chip). And then put the sample into rinse 1 (DI water) for 20 seconds and rinse 2 (DI water) for 30 seconds to remove the developer clean. We can check the pattern by microscope carefully. Completion degree of develop may be different from area to area. If develop is not completely done, we can develop sample for another 5 seconds. After that we check the pattern by scanning electron microscope again to make sure no residues remain. We can also measure the patterns by step profiler after develop. Fig. 4.2 shows the SEM image of cavity after developing resist.
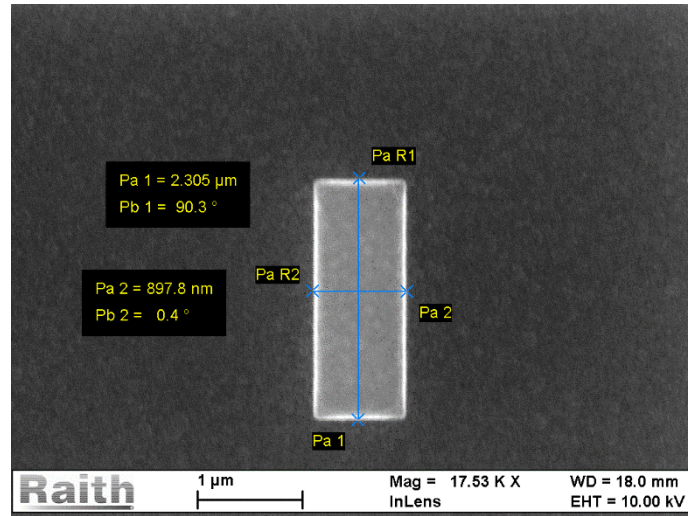
Fig. 4.2 Scanning electron microscope (SEM) image after develop

(f) Cr dry etching. We dry etching the Cr by ICP-RIE CE-S model from Ulvac company. Table 4-5 shows the condition of Cr dry etching.

(g) SiO_2 dry etching. We use RIE-10NR from Samco company to dry etching the SiO_2 layer. Table 4-5 shows the condition of SiO_2 dry etching. Different from previous recipe, we enlarge the RF power. Therefore, physical etching is intensified which can leave impurities on the surface by repelling the surface product more strongly.

(h) Dry etch InP and InGaAsP to develop cavity. This time we use PlasmaPro10 from Oxford company to do the InP and InGaAsP dry etching. Because it's the main process for cavity etching, we use H_2/CH_4 to dry etch the InP vertically which shows better result than Cl_2[43]. We set the recipe for 1 minute a cycle and after 5 cycle, we set several minutes for cooling down and restart etch. The etching rate of InP is about 80 nm/min and 50 nm/min for InGaAsP. Table 4-6 shows the dry etching condition of InP and InGaAsP. And Fig. 4.5 show the SEM image of developed cavity after dry etching.

Table 4-5 Condition of Cr and SiO_2's dry etching

Etching material	Cr	SiO_2
RF poIr (W)	400	120
Pressure (Pa)	5.0	2.0
Gas (sccm)	Ar/O_2/Cl_2 (10/25/40)	CHF$_3$/Ar (20/10)
Time	60 seconds	15 minutes
Etching rate	60 nm/s	27 nm/s

Table 4-6 Condition of dry etching for InP/InGaAs

Etching material	InP/InGaAs	O_2 cleaning	O_2 oxidization
Pressure (mTorr)	15.0	75.0	75.0
Gas (sccm)	H2/CH4 (45/15)	O_2（50）	O_2（50）
RF power (W)	120	40	80
ICP power (W)	100	0	0
Temperature (℃)	60	60	60
Etching rate	InP: 80 nm/min InGaAs: 50 nm/min		
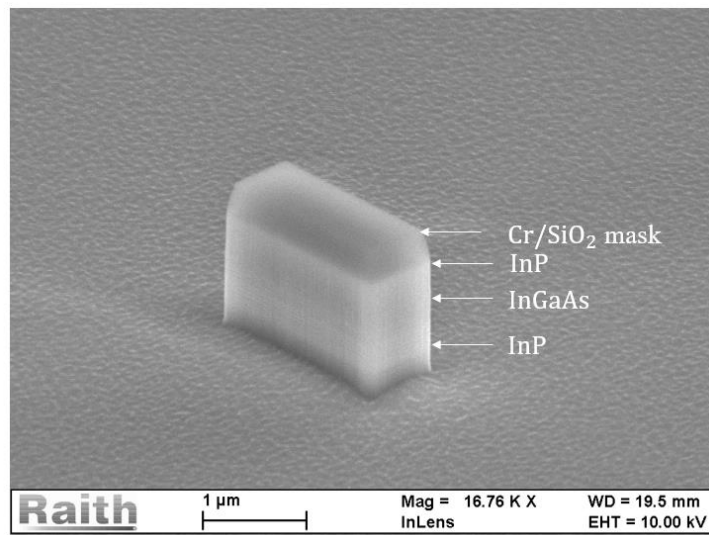
Fig. 4.3 Scanning electron microscope (SEM) image of the developed cavity
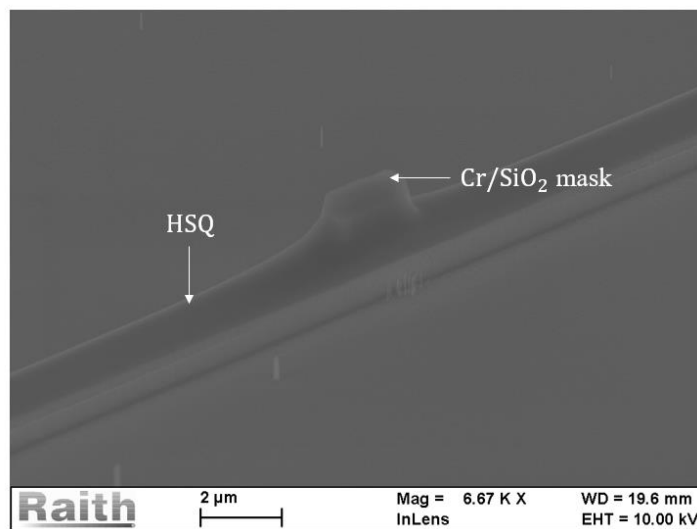

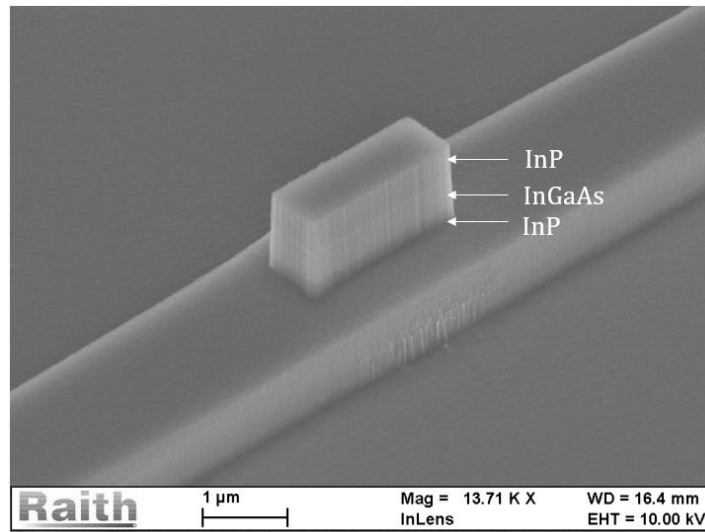Fig. 4.4 Waveguide coupled device after electron beam lithography and dry etching.

Fig. 4.5 Waveguide coupled device after surface treatment.

(i) Spin coating again. This time we use HSQ again as the resist for EB lithography. The condition of spin coating HSQ is shown in Table 4-5. Although after several steps of process, surface of sample is not clean as at beginning and spin coating of resist may not good, it is not recommended to remove resist and spin coat again even if part of sample is not well-distributed coated with resist. One should note that this time we set rotation per minute as 4000 rpm, which is larger than we set for cavity EBL.

(j) EB exposing and develop the waveguide. Since we should aim the cavity at the waveguide, we set some marks to do the alignment. The mark alignment is done through operation of controlling software. By recognizing marks on sample and setting alignment manually, the waveguide is draw under the cavity accurately.

(k) Dry etch InP and InGaAsP to develop waveguide. The thickness of waveguide is 750 nm, as shown in Table 4-1, from layer 6 to layer 9. About 120nm thick HSQ is capable to work as hard mask in this step. The condition of dry etching is the same as shown in Table 4-6. The SEM image after develop is shown in Fig. 4.4.

(l) Remove hard mask and surface cleaning. After dry etching by ICP-RIE, the cavity side is rough, which will increase the nonradiative radiation recombination efficiency on the surface proceeds. To avoid this, surface treatment of the cavity and waveguide is performed. At the same time, the mask is also peeled off. There are 5 steps in surface cleaning.

    (1) O_2 plasma oxidization. An O_2 plasma oxidization is generated by the RIE apparatus, thereby oxidizing the cavity surface. The condition of O_2 plasma oxidization is listed in Table 4-5. The lasting time is set as 1 minute.

    (2) Oxide removal. The oxide removal is done by diluted phosphoric acid (H_2PO_4:H_2O = 1:10) for 1minute. And use HCl : H_2O (1:20) to rinse for

39

about 10 seconds because InP will get oxidized even in DI water. It is recommended that this Step should be performed in dark environment where light does not strike the sample as much as possible in order to avoid unnecessary chemical reactions on the surface, making cavity surface rough.

The (1) and (2) should repeat for 3 times.

(3) Cr and SiO_2 hard masks removal. we remove Cr and SiO_2 hard masks by buffered HF (BHF) solution. 3 minutes are enough to remove 400 nm thick SiO_2. After this rinse the sample into in DI water for 1 minute.

(4) Slight InGaAs etching. We slightly wet-etch the InGaAs surface to remove impurities from the side of the active layer, InGaAs. Then we immerse for 5 seconds in dilute sulfuric acid H_2SO_4: H_2O_2: H_2O (1:8:5000). At last we rinse with DI water for 15 seconds and for another 60 seconds in another beaker.

(5) Ultrasonic cleaning. After InGaAs etching, the ultrasonic cleaning in acetone is done to remove remaining Cr, which is not dissoluble in BHF and sticky to sample surface. The condition is same as step (a).

(6) $(NH_4)_2S$ solution. We use 20% $(NH_4)_2S$ solution ($(NH_4)_2S$: H_2O = 1:4) to fill the dangling bond with S to prevent further oxidization by O_2. 30 minutes are enough for $(NH_4)_2S$ solution, and then rinse the sample into DI water. Fig. 4.5 shows the SEM image before and after surface treatment.

(m) SiO_2 deposition. As same as step (b). We first do the ultrasonic cleaning to clean the surface of sample. After that we deposit 30 nm thick SiO_2 insulator layer by PECVD.

(n) Ge & Ag deposition. The Ge and Ag are deposited by EB evaporator. Since the silver layer and SiO_2 layer shows weak adhesion, we deposit 2 nm thick Ge layer to enhance the relationship. Then we deposit thick silver film which is related to optical loss in cavity. To get better silver film, higher vacuum and deposition rate are needed. We deposit the silver when pressure in chamber is less than 3×10^{-5} Pa. On the other hand, the target (Ag) is heated by EB in high vacuum, and is melted into plasma and flies to the substrate upon the target, where a film is formed. Naturally, the evaporated material goes up straight in the vacuum, and thus, only the top of a 3D structure can be deposited effectively, while the sidewalls are free from evaporation. For better silver film, one should set the sample oriented at 45 ° to the axis of rotation of the holder because especially in a cavity with a rectangular shape such as a rectangle, metal is not deposited on the corner. Then the sample holder is rotated to deposit from a direction inclined 45 to 60 °, so that the cavity is oriented at 45 ° to the axis of rotation of the holder. In addition, target sample sets both Ge and Ag. Firstly, we deposit 2nm thick Ge with ±45 ° of the evaporation orientation. Then, we deposit 500nm thick Ag for 2 times at ±45 ° of the evaporation orientation. After that we rotate the sample

direction 90° with respect to the holder rotation axis and do another evaporation of 500nm thick Ag at ±45 ° of the evaporation orientation.

After deposition, RTA (Rapid Thermal Annealing) is done which can help increasing the grain size of Ag and reduces light scattering at the metal interface [44]. In this annealing, the temperature is raised to 400 ℃ for 8 minutes, and then heated for 1 minute. The SEM image of the waveguide coupled cavity structure after Ag deposition and RTA is shown in Fig. 4.6. we can see that Ag is also deposited on the corners.
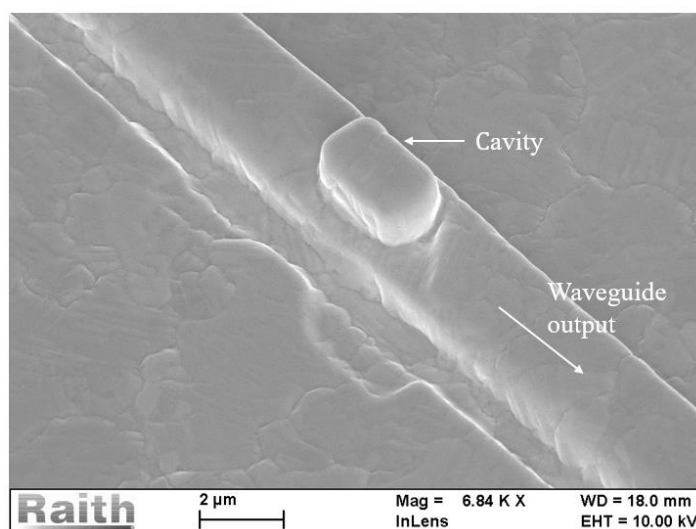
Fig. 4.6 Scanning electron microscope image （SEM）of fabricated waveguide-coupled metal-clad cavity.

4.2　Optimization of fabrication

4.2.1　Condition of HSQ

As talked before, the HSQ is very sensitive to operation condition. Any changes in the parameters and condition would cause unexpected affect in resist thickness and uniformity, which result in negative consequence during lithography. For example, the number of drips used in spin coating is very important and too much resist dripped onto the chip may cause difficulties in resist spreading. On the other hand, the rotation also has the effect on the thickness of HSQ. For we need to do another EB exposure of waveguide after dry etching the cavity, the thickness of HSQ takes great part. This time we should do the alignment by some marks set on the sample. The mark alignment is done through operation of controlling software. Thick HSQ may make it hard to alignment the waveguide accurately. We checked the resist thickness by Dektak and found that the thickness is about 250 nm at 3000 rotation per minute and 120 nm at
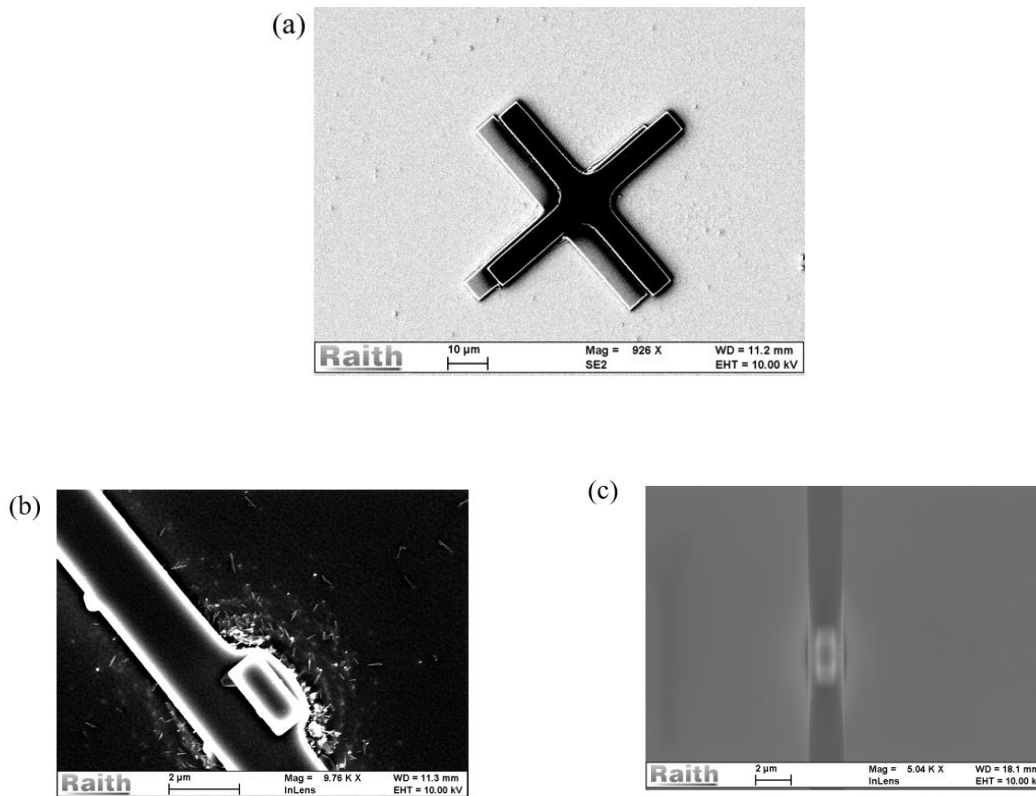
(a)

(b)

(c)

Fig. 4.7 (a) Mis matching of the marks. (b) and (c) Scanning electron microscope image （SEM）of waveguide-coupled cavity spin coat with 3000 rpm and 4000rpm (where the thickness of HSQ is 250 nm and 120 nm).

4000 rotation per minute. Fig. 4.7 (a) shows the mismatching of the alignment. Fig. 4.7 (b) and (c) shows the waveguide coupled device at different thickness of HSQ. It can be clearly seen that the waveguide and the cavity mismatched at the thickness of HSQ is 250 nm, and the waveguide is draw under the cavity accurately at the thickness of HSQ is 120 nm.

Also, the developing time of removing HSQ should be confirmed correctly. Too short time can't remove the resist clean. Fig. 4.8 shows the waveguide coupled cavity by putting the sample into the developer for 40 seconds. We can see the resist on the profile sides of the cavity and waveguide haven't been removed clean. More time should be done to clearly remove the resist because the resist adheres to the connect part of the waveguide and cavity is hard to remove. This time we put the sample into developer for 2 minutes to clearly remove the resist.
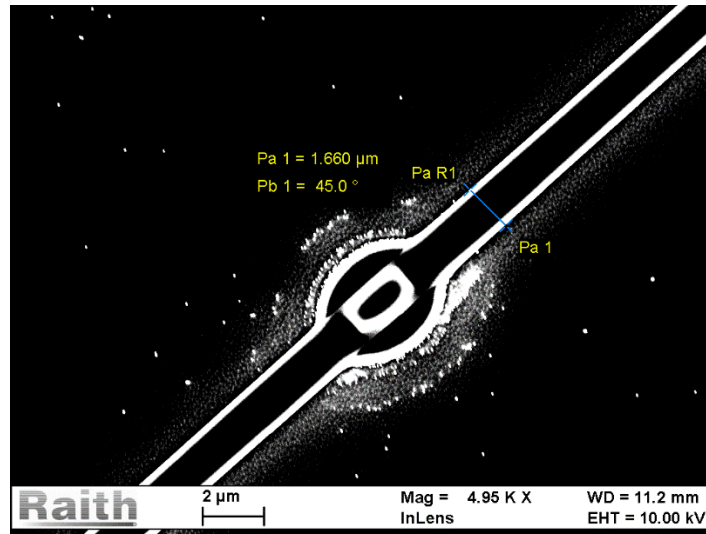
Fig. 4.8 Scanning electron microscope（SEM）image of waveguide-coupled cavity etching with remaining resist on profile sides.

4.2.2　Condition of SiO_2　dry etching

Table 4-7 Condition of Cr and SiO_2's dry etching

Etching material	SiO_2(before)	SiO_2(after)
RF power (W)	80	120
Pressure (Pa)	2.0	2.0
Gas (sccm)	CHF_3/Ar (20/10)	CHF_3/Ar (20/10)
Time	19 minutes	15 minutes
Etching rate	22 nm/s	27 nm/s

Table 4-7 shows the condition of SiO_2's dry etching we used before and we used after. As shown in Fig. 4.9 (a), the SiO_2 dry etching is performed using the previous condition. After etching, some polymers were formed on the chip surface as a reaction product. Therefore, if the next InP / InGaAs dry etching is performed while leaving it, the polymer will become a mask and it will be a problem that many pillars will be formed around the cavity. If a pillar-like structure remains around the cavity, subsequent metal deposition will not be successful which must be avoided. Therefore, in the previous research [32], sureface treatment was performed by removing the polymer attached to the InGaAs surface by wet etching the InGaAs layer on the surface by a small amount with sulfuric acid. In this study, the InP / InGaAs dry etching was performed after the surface treatment with sulfuric acid addition after the

43

dry etching of SiO_2. However, due to the large polymer remaining on the chip surface which can't be removed during surface treatment, some pillars have been formed on the surface as a result of InP / InGaAs dry etching as shown in Fig. 4.9 (a). Generally, by using sulfuric acid hydrolysis can remove impurities such as organic substances when the surface is a material with low reactivity to sulfuric acid hydrolysis such as InP [44]. While InGaAs is the sulfuric acid which will be removed easily, and this method should be avoided in this case.

To solve this problem, we use the new condition which enlarges the RF power as well as intensifying the physical etching. By repelling the surface product more strongly can etch the SiO_2 cleanly and no impurity on the surface. It is better to dry etching 2 more minutes to completely dry etching the SiO_2 film. After that, InP / InGaAs dry etching is performed as step (h) and the result is shown in Fig. 4.9 (b). The surface is clean and no pillars around the cavity.
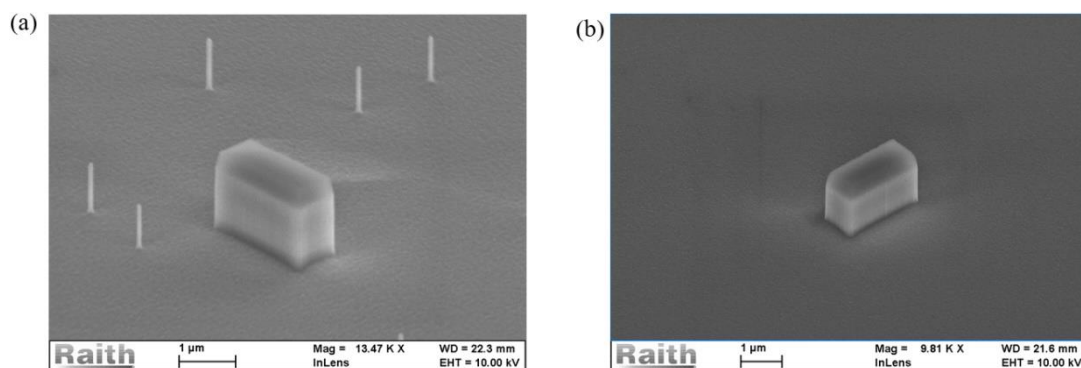
Fig. 4.9 (a) and (b) Scanning electron microscope（SEM）image of cavity with previous recipe and optimized recipe.

4.3 Summary

In this Chapter, we have performed the fabrication of the proposed waveguide coupled metal-clad cavity. Process flow and conditions of fabrication steps are investigated and improved, especially the condition of HSQ and SiO_2 dry etching. In order to accurately align the waveguide on the cavity, we set the rotation per minute to be 4000 rpm to form a 120 nm-thick HSQ film on the sample. To improve the surface condition after SiO_2 dry etching and InP/InGaAs dry etching, we decided the RF power to be 120 W, which can intensify the physical etching. By repelling the surface product more strongly can etch the SiO_2 cleanly and no impurity on the surface.

Chapter 5   Transmission characterization

In this Chapter, the transmission characterization of the fabricated waveguide coupled metal-clad cavity in Chapter 4 is measured.

In the following sections, we first introduce the setup of transmission measurement. Then the measurement results are given and analyzed in detail, which proves the numerical simulation in Chapter 3. At last, a brief summary is made.

5.1   Measurement setup

Fig. 5.1 shows the schematic of the experimental setup. A wavelength-tunable laser is used to generate continuous-wave light from 1477 nm to 1563 nm. The light passes through the polarization controller and is injected into the InP device via a lensed fiber . The output light is coupled to another lensed fiber and detected by a photodetector. For the measurement, the sample is cleaved into 1-mm-long devices and mounted on the copper plate.

We utilize a CCD camera to find the position of the waveguide and align it with the input and output fibers. First, we use a red laser pointer to input light from the input fiber. Through the camera, we can see the light hit the surface of the chip. We adjust the vertical position of the fiber, so that the red light illuminates exactly at the top edge of the waveguide facet. After that, we repeat the same procedure at the output fiber to make sure preliminary alignment is done.
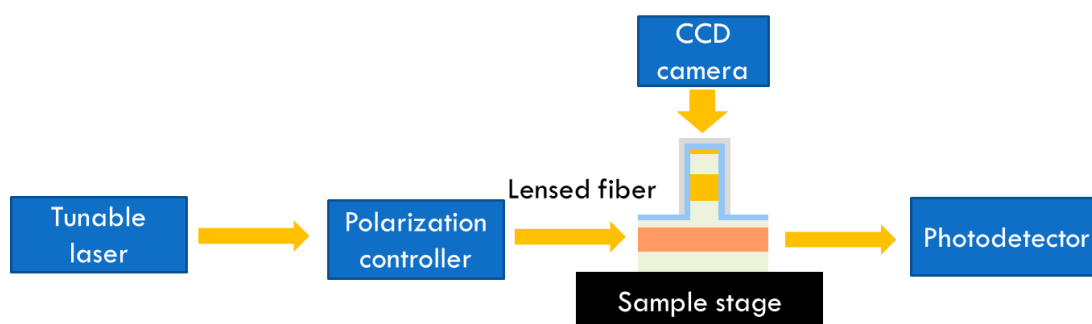
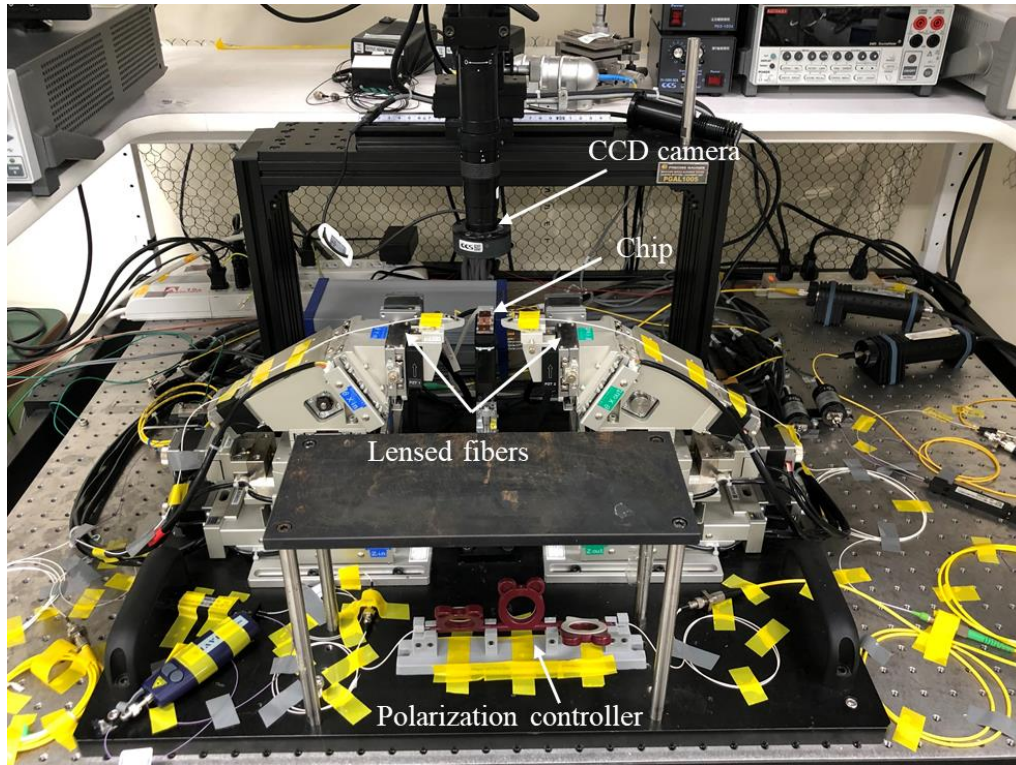

Fig. 5.1 Schematic of the experimental setup

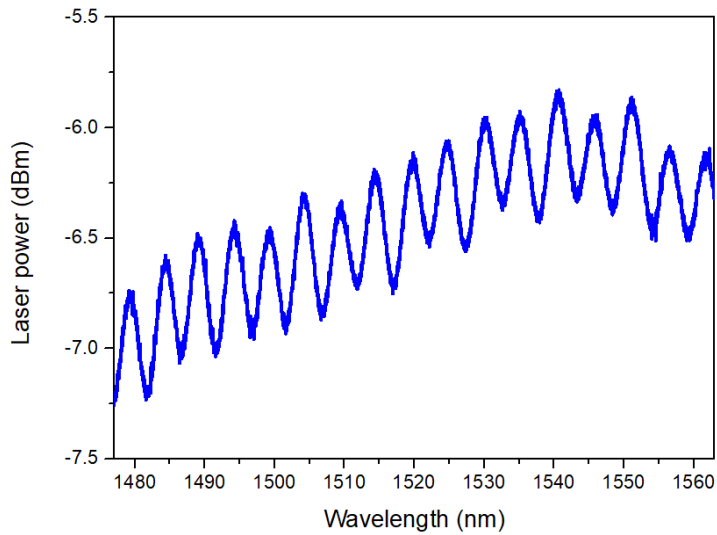Fig. 5.2 Measurement setup of waveguide-coupled cavity

Fig. 5.3 Measured spectrum of the monitored input light to the device

Fig. 5.3 shows the measured spectrum of the input light to the device. Since the monitored power shown in Fig. 5.3 is 10% of the actual input power to the device, the actual input power is around 3 dBm.
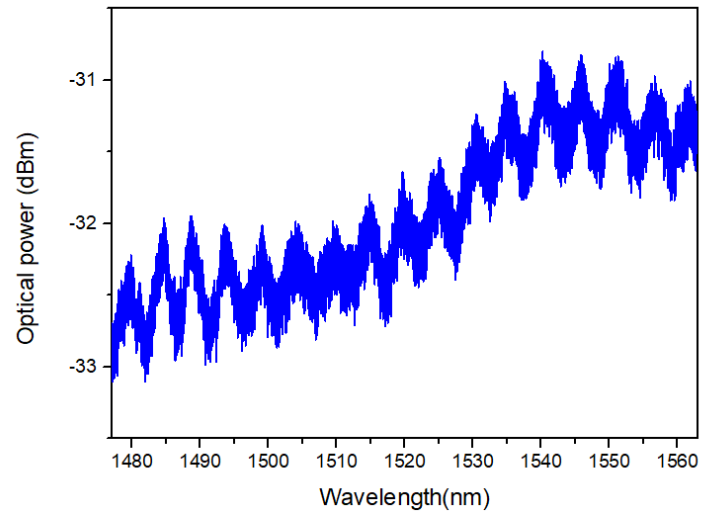
5.2 Measurement result

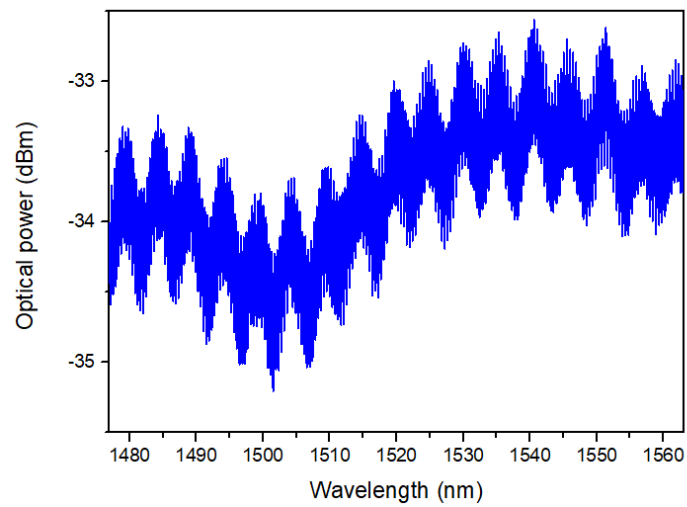Fig. 5.4 Measured spectrum from output waveguide (waveguide structure without cavity)

Fig. 5.5 Measured spectrum from output waveguide (waveguide coupled cavity structure)
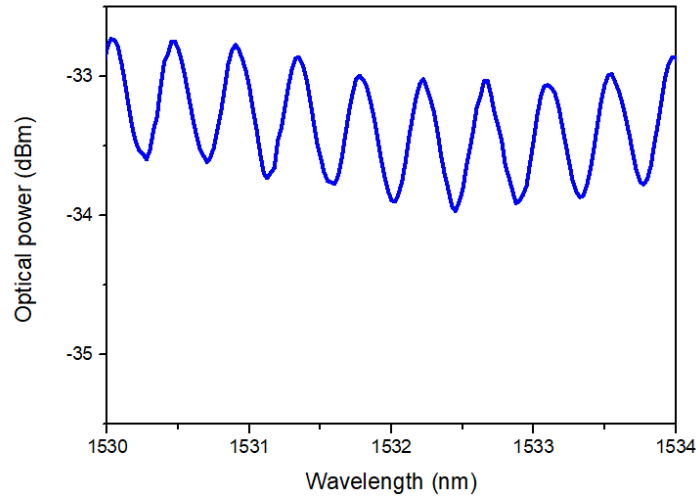
Fig. 5.6 Measured spectrum of the Fabry-Perot resonance

Fig. 5.4 shows the measured spectrum of the optical power from the output waveguide (waveguide structure without cavity). Fig. 5.5 shows the measured spectrum of the optical power from the output waveguide (waveguide coupled cavity structure). The waveguide structure without cavity shows a similar spectrum to the input light. Compare with the structure without the cavity; we can see a clear resonance pick as shown in Fig. 5.5.

To see it clearly, we amplify one part of the measured spectrum in Fig. 5.5. As shown in Fig. 5.6, we can confirm a finer oscillation with a period of 0.4 nm, which is mainly because the reflectivity at each facet between the waveguide and air is about 0.35. Thus, the waveguide itself can be seen as a Fabry-Perot resonator.

The measured transmission spectrum of the fabricated waveguide-coupled metal-clad cavity is shown in Fig. 5.7. Fig. 5.7 (a) shows the measured transmission spectrum for cavity length is 2.1 µm. The resonance pick is at 1485 nm, and the extinction ratio is 1 dB. Fig. 5.7 (b) shows the measured transmission spectrum for cavity length is 2.3 µm. We can see an obvious resonance pick at about 1500 nm. Moreover, the extinction ratio is 1.5 dB. Obviously, the optimized one shows a better result, which also agrees with the simulation results in Chapter 3. For comparison, Fig. 5.8 shows the simulated transmission spectrum. The resonance wavelength of the simulation result is at 1495 nm, which agrees with the measurement result. Thus, we can confirm that the light is coupled to the cavity at the resonance wavelength.
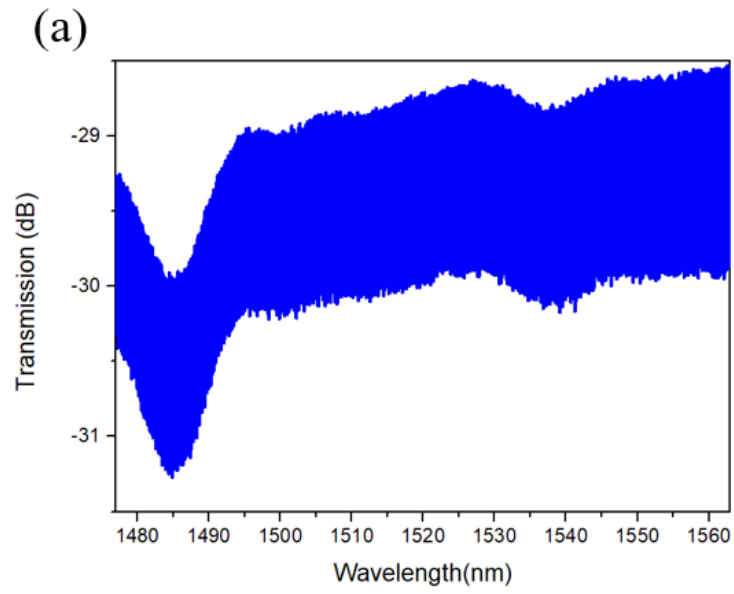
Fig. 5.7 (a) Measured transmission spectrum of the fabricated waveguide-coupled metal-clad cavity (L = 2.1 μm).

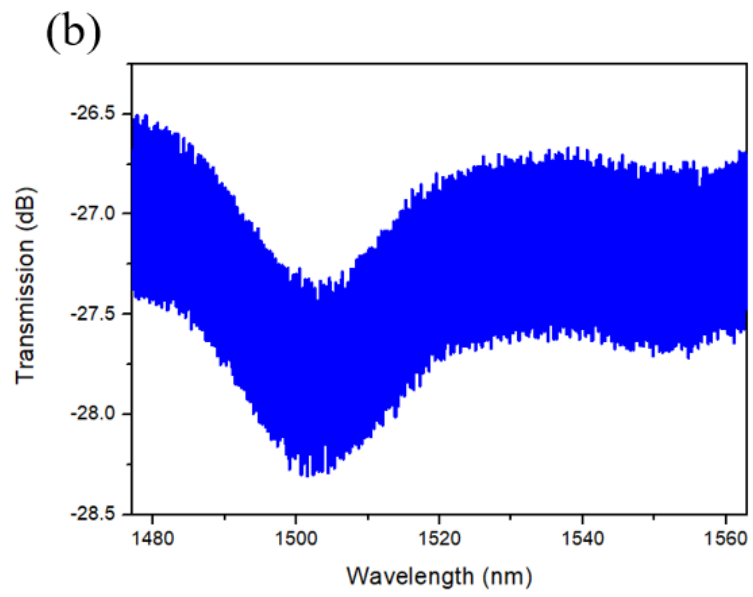Fig. 5.7 (b) Measured transmission spectrum of the fabricated waveguide-coupled metal-clad cavity (L= 2.3 μm).
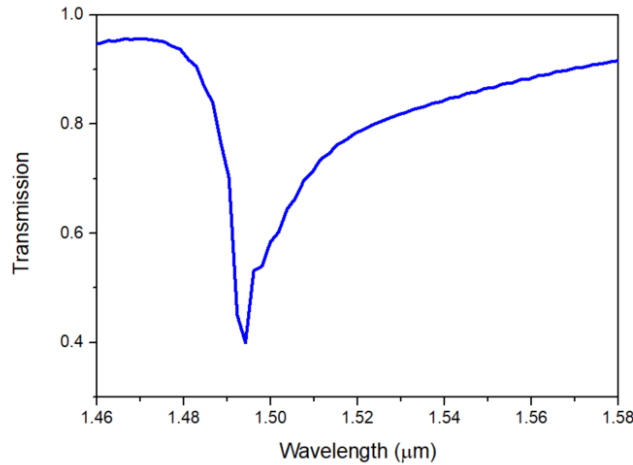
Fig. 5.8 Simulated transmission spectrum

The reduction in extinction ratio compared with the simulation result is attributed to several reasons. First, we have deposited a thick silver film to reduce the optical loss in the cavity, which may also have led to large metal loss to the input and output light. Second, the extra scattering in the lateral direction should reduce the extinction ratio.

5.3 Summary

In this Chapter, we use the sample fabricated in Chapter 4 to evaluate the transmission characteristic of the waveguide coupled cavity. We demonstrate that the light coupled to the cavity at the resonance wavelength of 1500 nm, which agrees with our FDTD simulation results. For comparison, we measured the transmission characteristic of waveguide coupled cavities with different cavity lengths. The optimized structure shows better results than the previous one. The measured extinction ratio is 1.5 dB. The decrease in the extinction ratio compared with simulation result is attributed to the metal loss and the extra scattering. For further optimization, firstly, we need to adjust the widths of the cavity and waveguide to minimize the scattering. Secondly, the fabrication process needs to be improved. Last but not least, a new structure of the waveguide coupled metal-clad cavity should be discussed to optimize the transmission characterization further.

Chapter 6   Design and fabrication of horn-shaped metal-clad cavity coupled to InP waveguide

As talked before, the resonance in the cavity failed to get in measurement mainly due to the low transmission and Q factor in previous work. For further optimization, we propose the horn-shaped cavity structure, which can maximize the Q factor and minimize scattering loss by using a 3D-FDTD method.

This chapter will first explain the principle of the horn-shaped metal-clad cavity. Next, the digital design of the metal-clad cavity coupled to the InP waveguide will be introduced. The 2D-FDTD simulation results show enhancement of Q factor and transmission and 3D-FDTD simulation results show similar answers as 2D-FDTD results. The calculation of the Q factor is also discussed, as well. After that, the modulator performance will be briefly introduced. Lastly, the fabrication of the horn-shaped cavity will be discussed.

6.1   Effect of insulator thickness to quality factor

Firstly, we studied the effects of SiO_2 insulator thickness on cavity performance [32]. The size of cavity is fixed to $L = 1.6$ μm, $W = 1$ μm, $L/R = 1.25$ and the coated metal is silver. It is said that the thickness of SiO_2 is another important factor that affects device's performance remarkably. In Fig. 6.1 (a), we can see Q factor is sensitive to the SiO_2 thickness. This time the refractive index of SiO_2 is 1.45, which is far below 3.53 of InGaAs. Along longitude direction, the interface of SiO_2 and InGaAs in front of silver mirror reflects light which can decrease the metal absorption. On the other hand, thick SiO_2 causes extra scattering, which increases the loss of the cavity.
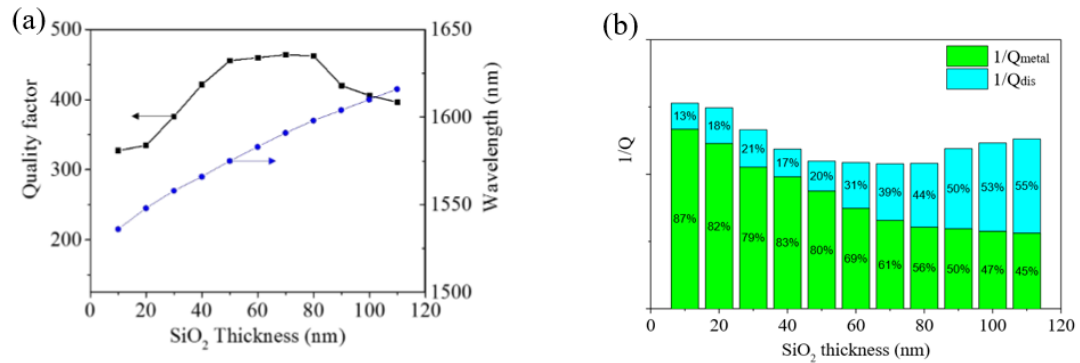

Fig. 6.1 (a) Quality factor and resonating wavelength as a function of thickness of SiO_2. (b) Fraction of $1/Q = 1/Q_{metal} + 1/Q_{dis}$, corresponding to metal absorption and radiation loss, respectively, as a function of SiO_2 thickness [32].

SiO_2 thickness also has great effect to Q factor. The quality factor can be written as $1/Q = 1/Q_{metal} + 1/Q_{dis}$, where $1/Q_{metal}$ and $1/Q_{dis}$ relate to metal-absorbed loss and radiation loss, respectively. Fig. 6.1(b) shows the fraction of $1/Q_{metal}$ (corresponding to metal absorption loss) and $1/Q_{dis}$ (corresponding to radiation loss) as a function of SiO_2 thickness. The height of column relates to power dissipation rate. The higher, the more lossy. We can see clearly the loss is almost induced by metal when SiO_2 is very thin which also shows low quality factor. As talked before, SiO_2 layer works like a half mirror which reflects the light, decreasing the metal absorption and its reflectivity increases at the range. Therefore, both absolute value and fraction of metal (green part of column) induced loss go down. On the other hand, inside the SiO_2 layer, there is no refractive index difference in vertical direction, meaning that no confinement in vertical direction. So the guided mode escapes to the bottom. As we can see, the radiation loss goes up as the thickness of SiO_2 becomes larger.

So there still need some methods to both decrease the metal loss and the radiation loss by the effect of SiO_2 thickness to the cavity performance.

6.2   Horn-shaped metal-clad cavity

Fortunately, recent work on horn-shaped metal-clad cavity for on-chip light source application showed the possibility of reducing the plasmonic losses and improving the mode confinement by optimizing the slope angle of the SiO_2 insulator layer [33]. Fig 6.2 shows the schematics of the proposed horn-shaped metal-clad resonator.
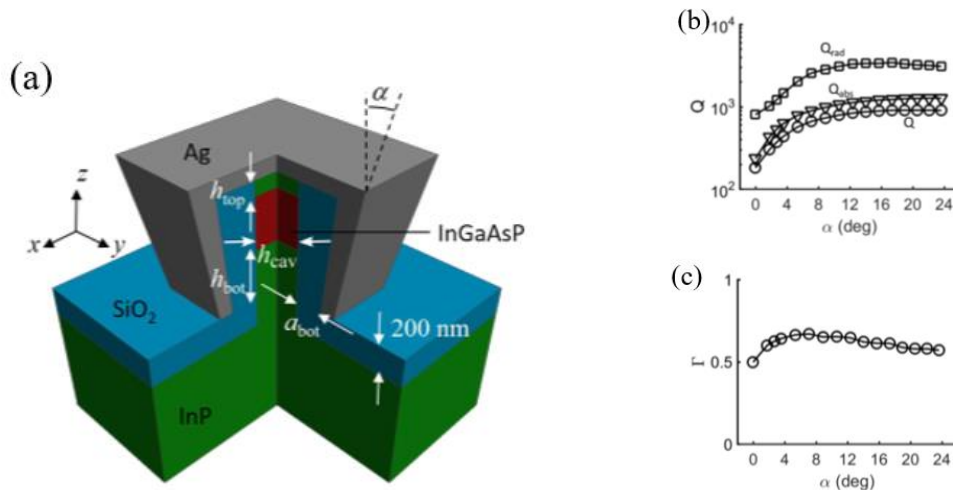

Fig. 6.2 (a) Schematics of the proposed horn-shaped metal-clad resonator. (b), (c) The properties of the horn-shaped metallic-clad cavity for different slope angles α. (b) Quality factor (Q: total, Q_{abs}: absorption, Q_{rad}: radiation). (c) overlap factor Γ [34].

The Q factor can be decomposed into the metal absorption and radiation loss ($Q^{-1} = Q_{abs}^{-1} + Q_{rad}^{-1}$) [34,35]. This can be observed in Fig. 6.2 (b). The stable current density distribution at the metallic layer near the cavity indicates the energy absorption Q_{abs} due to the spatial spread of the mode. Q_{rad} is indicated by the leaky electric field under the cavity that causes energy to radiate into the InP substrate through the dielectric passage. The wider cladding region near the cavity reduces optical absorption, and the narrowing passage near the bottom enhances the vertical confinement [36]. By adjusting the parameter α for the sloping angle provides another leverage to affect the Q_{abs} and Q_{rad}, which will lead to further enhancement of the overall Q factor.

As shown in Fig. 6.2 (b), Q_{rad} and Q_{abs} increase due to the higher confinement of energy in the cavity. The position of the resonance mode moves upward toward the wider cladding region in the cavity and reduces the leakage as well as metallic absorption. Fig. 6.2 (c) shows the overlap factor Γ. Γ was shown to decrease slightly for $\alpha > 8°$ because the mode spreads into a larger cladding region. By increasing the cladding slope angle from 0 to 16°, the Q factor increased from 50 to 900 and Purcell factor increased from 18 to 135, respectively. This approach can serve as a design guide toward implementing ultra-compact and cost-efficient on-chip metal-clad devices [45].

6.3   Numerical design and simulation result of horn-shaped metal-clad cavity coupled to InP waveguide

We implement this horn-shaped structure concept to a compact cavity integrated on an InP waveguide, and optimize the structure to maximize the Q factor and minimize scattering loss. Fig. 6.3 shows the schematic of the horn-shaped metal-clad cavity considered in this work. The primary layer profile is the same as Chapter 3.
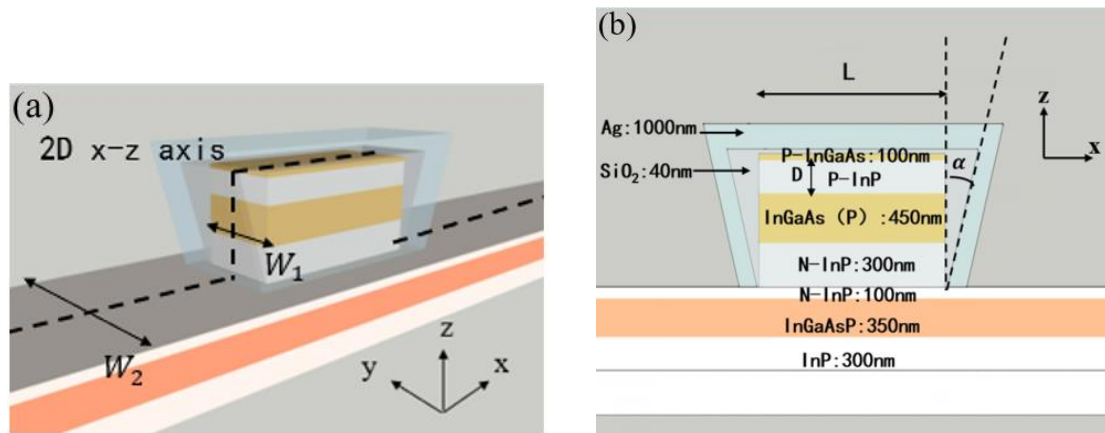

Fig. 6.3 (a) 3D Schematic and (b) the cross-sectional view at *x-z* plane of the horn-shaped metal-clad resonator.

This time we mainly focus on the slope angle α of SiO$_2$ as an important parameter. The device is analyzed by the finite-difference time-domain (FDTD) method. Since the slope angle also has the same effect at x-z direction as well as y-direction, we will first optimize the slope angle α through 2D FDTD simulation at x-z direction as shown in Fig. 3.3 (a). This part can save much simulation time because using 3D-FDTD will take much more time than 2D-FDTD. Then we confirm the performance of the optimized structure by full 3D simulation. In the 3D simulation part, we will also focus on the calculation of Q factor. Usually, the calculation of high Q factor cavities cost a long time, but if we can figure out the decay rate of the certain mode, we can interrupt the calculation halfway. In this research, the calculation is carried out precisely in this way. In detail, we will also calculate the Q_{metal} and $Q_{radiation}$ extracted by integrating the Poynting vector at the metallic boundaries and compare it with the 2D-FDTD simulation result.

6.3.1 2D-FDTD simulation (Optimize the slope angle)

In Chapter 3, we maximized the Q factor from 296 to 535 as well as the extinction ratio from 1.98 dB to 4.32 dB. We start from the optimized structure and investigate the effect of nonzero slope angle α. As previous research purposes, by optimizing the slope angle of SiO$_2$ insulator layer, the possibility of reducing the plasmonic losses and improving the mode confinement.
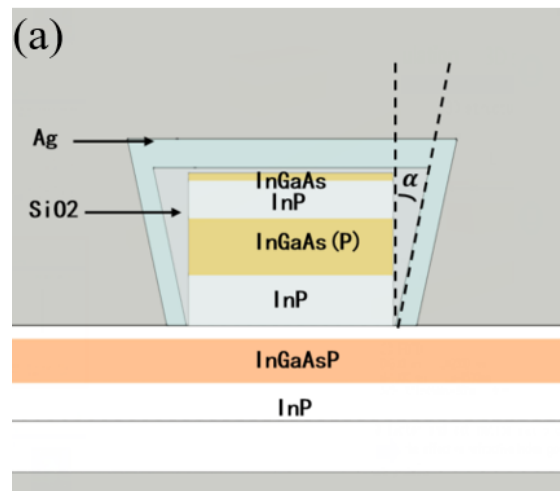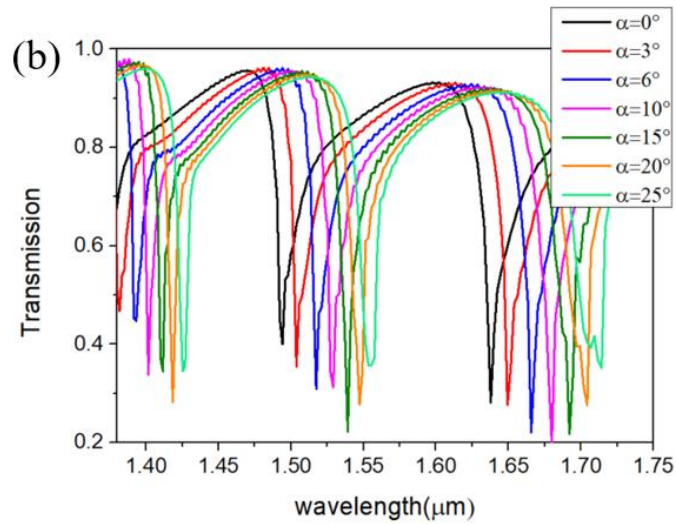
Fig. 6.4 (a) Schematic image and (b) Transmission spectrum for various values of α ($L = 2.3$ μm, $D = 300$ nm). The resonance wavelength shifts with the increase in α, while the peak transmission remains nearly constant.

The transmission spectra for various values of α are plotted in Fig. 6.4 (b) for $L = 2.3$ μm and $D = 300$ nm as optimized in previous section. We can see that the resonant wavelength shifts with the increase in α, while the peak transmission remains nearly constant. The reason why peak transmission remains is that the cavity structure doesn't change (only adjusting the slope angle of SiO_2 insulator layer) while the resonant wavelength shifts because of the resonance mode shifting with slope angle. Fig. 3.10 shows the Q factor as a function of α. The maximum Q factor of 1054 is obtained at $\alpha = 15°$. One maybe confused why Q factor doesn't keep increasing with the slope angle but get maximum at 15°. The explanation will be shown in 3D-FDTD simulation.
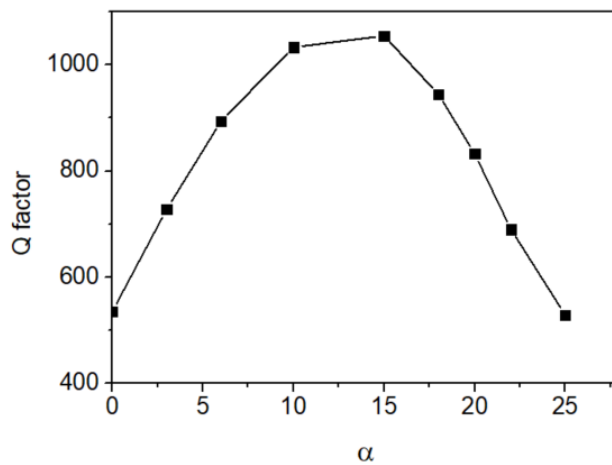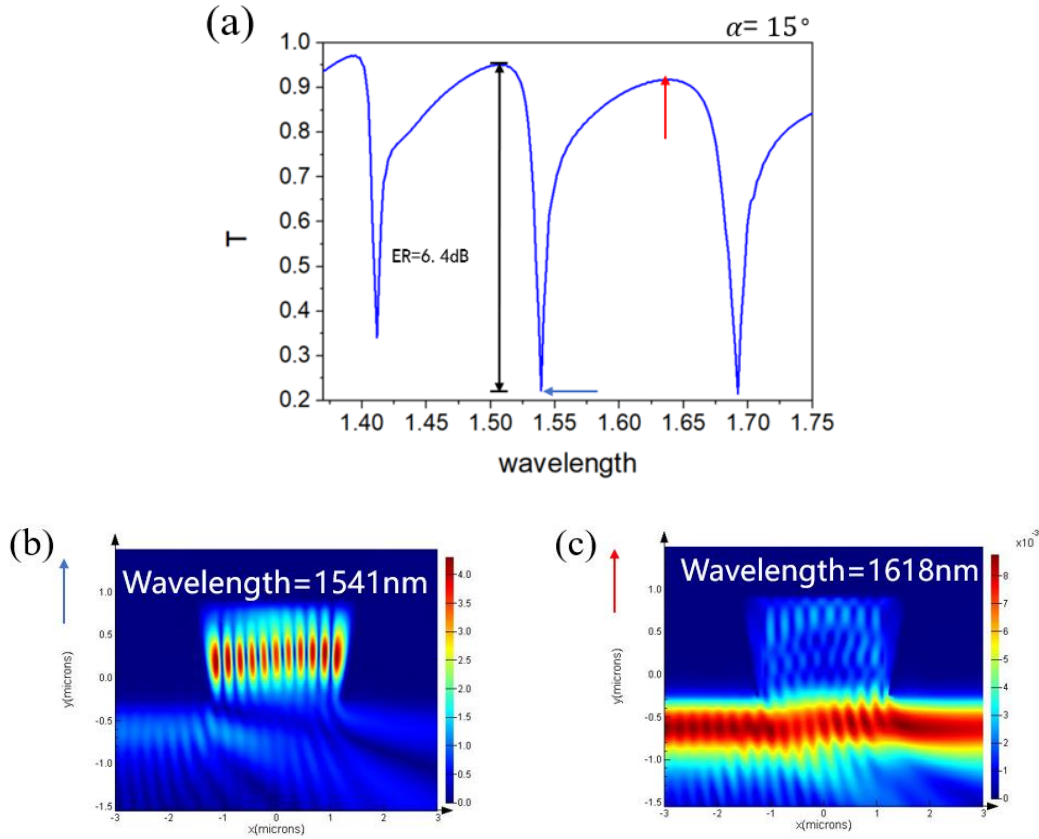

Fig. 6.5 Q factor of resonant mode as a function of α.

55

Fig. 6.6 (a) Transmission spectrum for L = 2.3 μm, D = 300 nm, and α = 15°. (b) Electric field distribution at resonance wavelength (1554 nm) (c) Electric field distribution at non-resonance wavelength (1618 nm)

Fig. 6.6 (a) shows the transmission spectrum for the optimized case: L = 2.3 μm, D = 300 nm, and α = 15°. In this case, the extinction ratio of 6.4 dB and Q factor of 1054 is obtained. Fig. 6.6 (b) and (c) show the simulated electric field distributions at a resonant wavelength (1541 nm) and a non-resonating wavelength (1618 nm), respectively. We can see that at the resonant wavelength (1541 nm), the incident light is trapped inside the cavity and eventually absorbed by Ag, while the light is transmitted through at non-resonance wavelength (1618 nm).

6.3.2 3D-FDTD simulation

The 3D FDTD simulation is carried out for the optimized structure (L = 2.3 μm, D = 300 nm). As shown in Fig. 6.3 (a), we set the cavity width to be W_1 = 1 μm and waveguide width to be W_2 = 1.5 μm.

In order to find out the proportion of power that coupled into waveguide for this horn-shaped cavity, we look into the detailed component of overall Q factor. Considering steady lasing state of a cavity. The loss during the resonating is consist of two part, as shown in Fig. 6.7.

$$E_{loss} = E_{metal} + E_{radiaton} \tag{6-1}$$

Where E_{metal}, $E_{radiaton}$ represents absorption by metal and radiation into waveguide, respectively. From the calculated Q factor, contributions from the metallic loss and
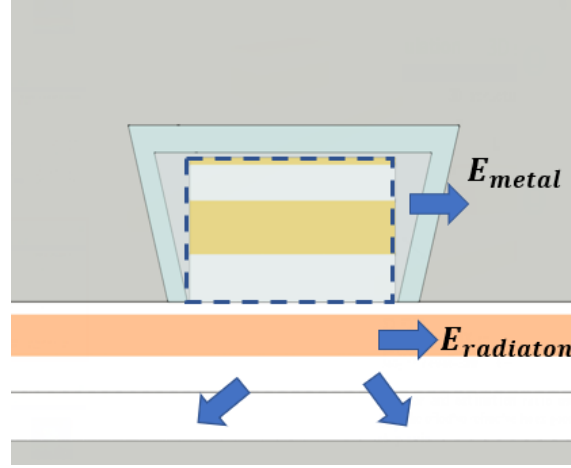

Fig. 6.7 Energy loss from cavity

radiation loss are extracted by integrating the Poynting vector at the metallic boundaries and using [38]

$$\frac{1}{Q} = \frac{1}{Q_{metal}} + \frac{1}{Q_{radiation}} \tag{6-2}$$

And the Q factor of a resonant cavity is defined as

$$Q = \frac{2\pi f_0 E}{P} \tag{6-3}$$

Where the E is the stored energy inside the resonator, $P = -dE/dt$ is the power dissipation rate, f_0 is the resonant frequency. From this equation, the optical energy E can be written as a function of time t.

$$E(t) = E(0)e^{-\frac{2\pi f_0}{Q}t} \tag{6-4}$$

The loss of energy E_{loss} is written as

$$E_{loss} = E(0) - E(t) = \frac{2\pi f_0}{Q}t \cdot E(0) \tag{6-5}$$

By combining Equation 6-4 and Equation 6-5, we get

$$E_{loss} = \frac{2\pi f_0}{Q} t \cdot E(0) = \left(\frac{1}{Q_{metal}} + \frac{1}{Q_{radiation}} \right) 2\pi f_0 t \cdot E(0)$$

$$\equiv E_{metal} + E_{radiaton} \qquad (6\text{-}6)$$

The E_{metal} and $E_{radiaton}$ can be calculated through 3D-FDTD simulation. As shown in Fig. 6.8, we set the cube S_1 cover the whole cavity, which is a bit larger than silver coatings. Similarly, the cube S_2 is set inside cavity which is smaller than silver coatings. The pointing vector is calculated by $\vec{P} = \vec{E} \times \overrightarrow{H^*}$. Surface integrals of vector field $\vec{P}$ represents the power passes through the cube.
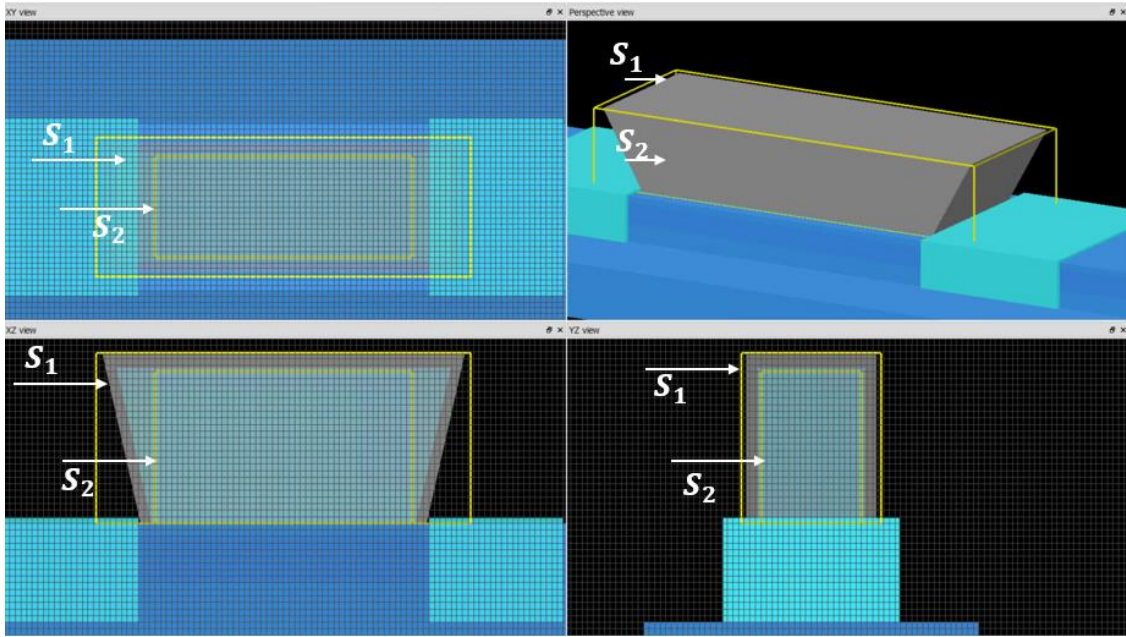
Fig. 6.8 Schematic of energy loss calculation

The calculated results are shown in Fig. 6.9. We can see both Q_{metal} and $Q_{radiation}$ increase with increasing angle due to the higher confinement inside the cavity as talked before. The optical absorption also reduces by adjusting α. When α exceeds 15°, however, the vertical confinement becomes lower, and the extra scattering becomes even stronger. $Q_{radiation}$ reduces rapidly due to the extra scattering. And the Q_{metal} almost keep stable. A trade-off point between $Q_{radiation}$ and Q_{metal} is obtained at α = 15°, where the maximum Q factor reaches 408. The maximum Q factor also agrees with the result of the 2D simulation.
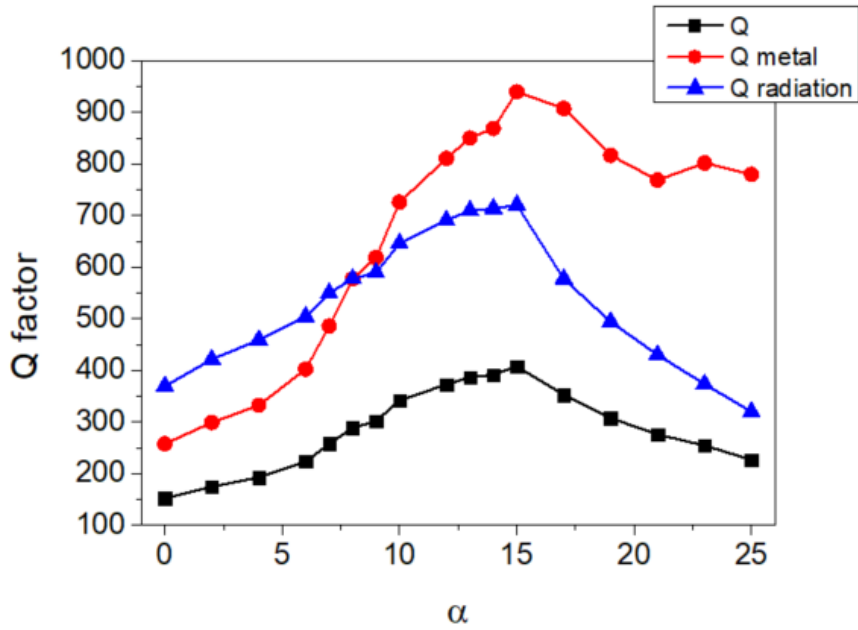
Fig. 6.9. Total Q, Q_{metal}, and $Q_{radiation}$ as a function of α, derived from 3D FDTD simulation ($L = 2.3$ μm, $D = 300$ nm).
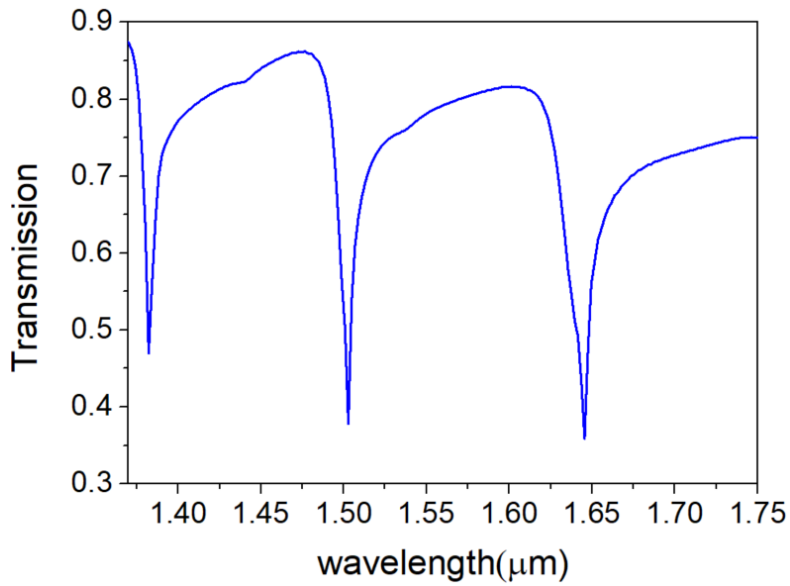
Fig. 6.10. Transmission spectrum of the best case: $L = 2.3$ μm, $D = 300$ nm, $W_1 = 1$ μm, $W_2 = 1.5$ μm, and $\alpha = 15°$. The extinction ratio is 3.9 dB.

Fig. 6.10. shows the transmission spectrum for the best case: $L = 2.3$ μm, $D = 300$ nm, $W_1 = 1$ μm, $W_2 = 1.5$ μm, and $\alpha = 15°$. In this case, the extinction ratio is 3.9 dB, and Q factor is 408. The reduction in Q factor compared with the 2D result may attribute to the extra scattering in y-direction. For further optimization, we need to adjust the widths of the cavity and waveguide to minimize the scattering.

6.3.3 Application to modulator

By applying a reverse bias to modulate the refractive index of the InGaAsP active layer inside the cavity, it could be used as a resonant modulator. To study the applicability to a waveguide modulator, we investigate the resonant wavelength shift under the refractive index change in the active InGaAsP layer. Fig. 6.11 (a) shows the simulated transmission spectrum for different values of the refractive index of the InGaAsP layer. As a result, input light at 1502 nm can be modulated by 3.2 dB with the internal loss of 1.5 dB. Fig. 6.11 (b) and (c) show the simulated electric field intensity distributions at 1502 nm for the cases of $n = 3.50$ and 3.51, respectively. We can see that at the resonant wavelength, the incident light is trapped inside the cavity and eventually absorbed by Ag.
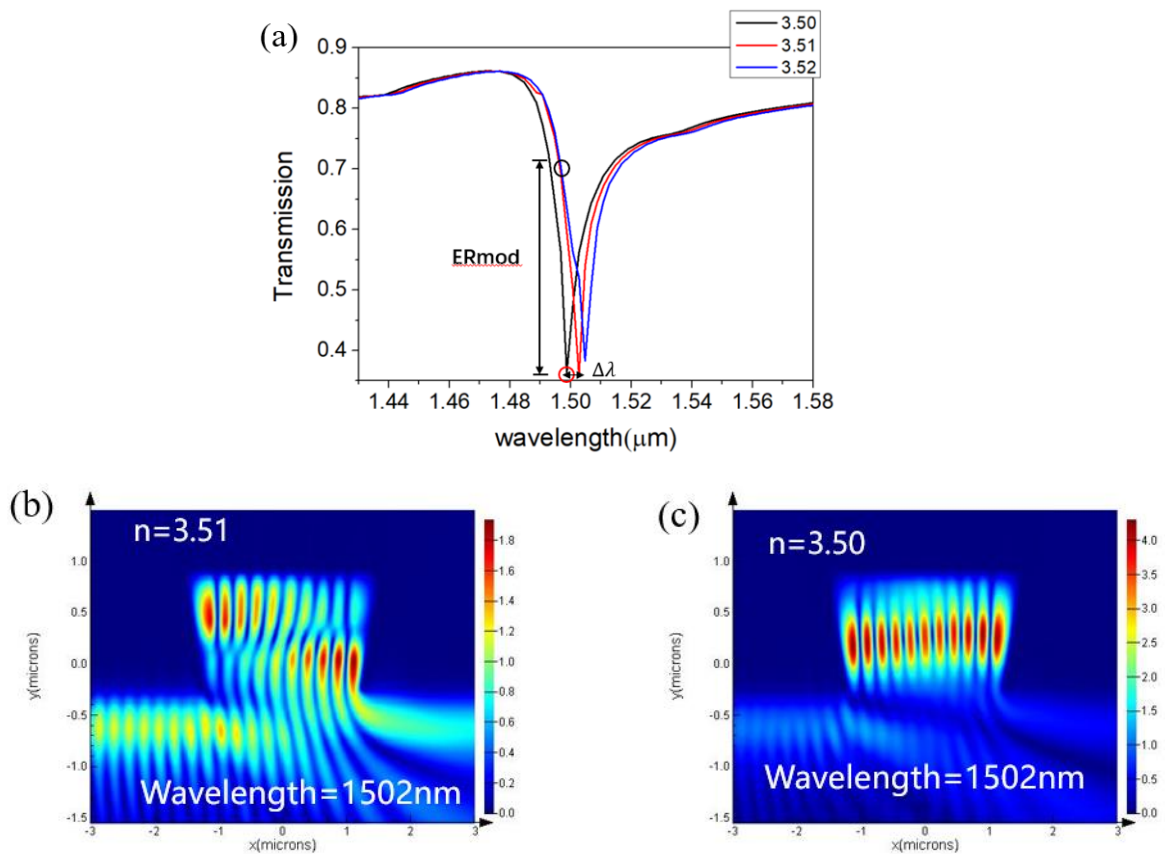

Fig. 6.11 Transmission spectrum when the refractive index of the active InGaAsP layer n is 3.50, 3.51 and 3.52 (a), and electric field distribution at 1502 nm for the case of $n = 3.50$ (b) and 3.51 (c).

6.4   Horn-shaped SiO_2 layer deposition

This part focus on forming the horn-shaped SiO_2 layer. This time we use the EB evaporator to deposit the horn-shaped SiO_2 film as an insulator layer in the proposed design. The target (SiO_2) is heated by EB in high vacuum below 6.7×10^{-5} Pa as possible, which is melted into plasma and flies to the substrate upon the target, where a film is formed [46]. As the nature of this process, the evaporated material goes up straight in the vacuum because of the long mean-free path of a few tens of centimeters. Thus, only the top of a 3D substrate can be deposited, while the profiles are free from evaporation. Fig. 6.12 can schematically illustrate this feature. As we can see, the dashed line directs the shadow area where cannot be deposited with the target material.
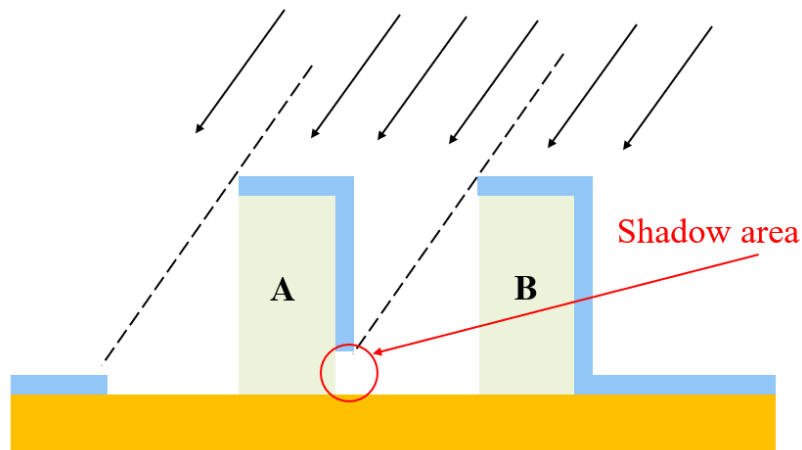

Fig. 6.12 Oriental feature of EB evaporation. The black arrows indicate the direction of evaporation. And the dashed line directs the shadow area.
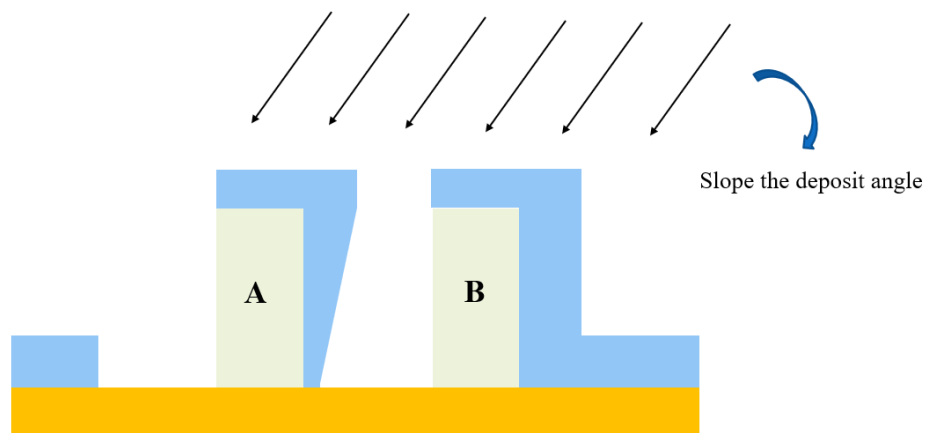

Fig. 6.13 Schematic of horn-shaped SiO_2 layer deposition.

This time we utilize this feature to deposit the horn-shaped SiO_2 layer. As shown in Fig. 6.13, we first deposit the target material to some degree to ultimately form the SiO_2 film either on top of the structure or on profile sides. Then we slope the deposit angle to form a thicker SiO_2 film on sidewalls of the fabric to make the horn-shaped SiO_2 layer. One should note that the deposit angle needs to be changed gently to develop the SiO_2 film smoothly. Too fast may cause the insulator layer formed worse. Fig. 6.14 shows the SEM image of the cavity after SiO_2 deposition. After the SiO_2 deposition, about 300 nm thick SiO_2 formed on the top of the cavity, so we should dry etching the top of the SiO_2 layer as shown in step (g) in Chapter 4. As shown in Fig. 6.14 (a), the horn-shaped SiO_2 film formed at both sidewalls after the deposition, and the thick SiO_2 formed on the top of the cavity. Fig. 6.14 (b) shows the SEM image of the cavity with horn-shaped SiO_2 film after top SiO_2 dry etching.
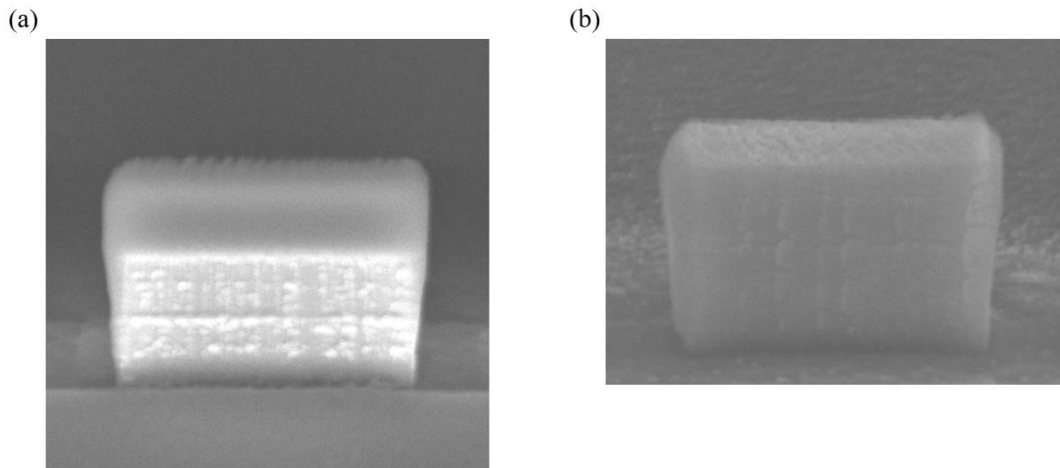
(a)

(b)

Fig. 6.14 (a) The SEM image of the cavity after SiO_2 deposition. The top of the structure has thick SiO_2 layer.
(b) The SEM image of the cavity with horn-shaped SiO_2 film after top SiO_2 dry etching.

6.5 Summary

In this chapter, I have introduced the detailed design and simulation result of the 2.3-μm-long horn-shaped metal-clad cavity integrated with an InP waveguide. Two essential parameters have been optimized through FDTD simulation. By adjusting the slope angle of the SiO_2 insulating layer, we demonstrated that the Q factor could be enhanced significantly from 152 to 408 in 3D FDTD simulation. Then we have shown the applicability of this structure to a compact modulator with an internal loss of 1.5 dB and the extinction ratio of 3.2 dB. We expect that the device performance could be further improved by optimizing the structure in the width dimension. The possibility of high-speed modulation is expected due to the low-resistance electrical contact of the metallic cavity. In the fabrication part, we successfully deposit the horn-shaped SiO_2 film by using the EB evaporator.

Chapter 7 Conclusion

In this research, we find new structures and further optimize the cavity structure to enhance the property of metal-clad cavity coupling to InP waveguide. The simulation results by the FDTD method shows the maximum of the Q factor and the transmission. Base on these results, we proposed an optimized design of the metal-clad cavity coupling to InP waveguide.

We first introduced small light emitters and confirmed the metallic cavity semiconductor nano-laser to be a light source for on-chip optical interconnects. However, as mentioned before, the emitting light to the substrate brings extraction and diffraction problems and low Q factor. The necessity of the waveguide coupled metal-clad cavity which can solve the common problems of metallic cavity laser has been reviewed. Although previous work has been done to make the metal-clad cavity coupling to InP waveguide, low Q factor and transmission cause the resonance in the cavity failed to get in a measurement. So this research is exactly focused on enhancing the property of metal-clad cavity coupling to InP waveguide to relived the problems.

We introduced the detailed design and simulation result of the 2.3-μm-long metal-clad cavity integrated with an InP waveguide. Two essential parameters have been optimized through FDTD simulation. By optimizing the length of the cavity and thickness of the upper InP cladding, we maximized the Q factor of the resonant mode as well as the extinction ratio. We investigated that the extinction ratio could be enhanced significantly from 1.98 dB to 4.32 dB. Also, the Q factor enlarged from 296 to 535 in 2D FDTD simulation.

We also improve the fabrication process, especially the condition of HSQ and SiO_2 dry etching. In order to accurately align the waveguide on the cavity, we set the rotation per minute to be 4000 rpm to form a 120 nm-thick HSQ film on the sample. To improve the surface condition after SiO_2 dry etching and InP/InGaAs dry etching, we decided the RF power to be 120 W, which can intensify the physical etching. By repelling the surface product more strongly can etch the SiO_2 cleanly and no impurity on the surface. The transmission characterization shows very good agreement between simulation and experiment.

We successfully get the measurement of the resonance in the cavity for the first time. We also demonstrate the optimized one shows a better result than the previous one. The resonance in the cavity of the optimized case is at 1500 nm, which agrees with the simulation result by FDTD. The measured extinction ratio is 1.5 dB.

To further enhance the Q factor at the resonance wavelength, we also numerically investigate a novel structure based on a horn-shaped metal-clad cavity, coupled to an InP waveguide. By adjusting the slope angle of the SiO2 insulating layer, we demonstrated that the Q factor could be enhanced significantly from 152 to 408. We

have then demonstrated the applicability of this structure to a compact modulator with an internal loss of 1.5 dB and the extinction ratio of 3.2 dB. We expect that the device performance could be further improved by optimizing the structure in the width dimension. The possibility of high-speed modulation is expected due to the low-resistance electrical contact of the metallic cavity. In the fabrication part, we successfully deposit the horn-shaped SiO_2 film by using the EB evaporator.

However, this research has several important issues to promote in the future.

● Measurement of the horn-shaped metal-clad cavity

Although we successfully deposit the horn-shaped SiO_2 film, we have not done the measurement of the fabricated structure due to the time-limited. The simulation results show significant enhancement of the Q factor and the extinction ratio. Also, the possibility of high-speed modulation is expected due to the low-resistance electrical contact of the metallic cavity. Further improvement of the fabrication of the horn-shaped SiO_2 deposition could be done in the future. The measured transmission characterization may show better results than the rectangular cavity.

● Further optimization of waveguide coupled cavity structure

As shown in 3D FDTD results, the reduction in Q factor compared with the 2D result may attribute to the extra scattering in the y-direction. For further optimization, we need to adjust the widths of the cavity and waveguide to minimize the scattering. Topology Optimization of Metal-clad Cavity Structure [44] also shows enhancement in Q factor. The new cavity structure can be discussed in the future.

Publication

International conference

Yuguang Wang, Yi Xiao, Mitsuhiro Watanabe, Takuo Tanemura, and Yoshiaki Nakano, "Horn-Shaped Metal-Clad Modulator Coupled to InP Waveguide", Compound Semiconductor Week 2019, Nara, May, 2019

Domestic conference

Yuguang Wang, Yi Xiao, Takuo Tanemura, and Yoshiaki Nakano, "オンチップ光配線に向けた InP 導波路結合型金属クラッド共振器デバイスの設計", 光エレクトロニクス研究会（OPE），慶應義塾大学，2018 年 12 月

References

[1] M. T. Hill and M. C. Gather, "Advances in small lasers," Nat. Photonics 8, 908 (2014).

[2] Miller, D. a. B. Rationale and challenges for optical interconnects to electronic chips. Proc. IEEE 88, 728–749 (2000).

[3] Ian O'Connor, Frédéric Gaffiot, "On-Chip Optical Interconnect for Low-Power," Ultra Low-Power Electronics and Design, Springer, pp. 21-39, 2004.

[4] M. Smit, J. van der Tol, and M. Hill, "Moore's law in photonics," Laser Photonics Rev., vol. 6, no. 1, pp. 1–13, 2012.

[5] D. A. B. Miller, "Device requirements for optical interconnects to silicon chips," Proc. IEEE, vol. 97, no. 7, pp. 1166–1185, 2009.

[6] S. E. Miller, "Integrated optics: An Introduction," Bell Syst. Tech. J., vol. 48, no. 7, pp. 209-2069, 1969.

[7] Saraswat, K. C. & Mohammadi, F. "Effect of Scaling of Interconnections on the Time Delay of VLSI Circuits." IEEE J. Solid-State Circuits 17, 275–280 (1982).

[8] A. Mizrahi, V. Lomakin, et al., "Low threshold gain metal coated laser nanoresonators," Opt. Lett. 33(11), 1261 (2008).

[9] K. Ding and C. Z. Ning, "Fabrication challenges of electrical injection metallic cavity semiconductor nanolasers,", Semicond. Sci. Technol. 28(12), 124002 (2013).

[10] T.H. Maiman, "Stimulated Optical Radiation in Ruby," Nature, vol. 187, no. 4736, pp. 493-494, 1960.

[11] Robert N. Hall, G. E. Fenner, J. D. Kingsley, T. J. Soltys, and R. O. Carlson, "Coherent Light Emission From GaAs Junctions," Physical Review Letters, vol. 9, no. 9, pp. 366-369, 1962.

[12] K. Iga, C. Kitahara, and Y. Suematsu, H. Soda, "GaInAsP/InP surface emitting injection lasers," Jpn. J. Appl. Phys., vol. 18, no. 12, pp. 2329-2330, 1979.

[13] R.E. Slusher, S.L. McCall, T. Tanbun-Ek, D.L. Coblentz, S.J. Pearton A.F.J. Levi, "Room temperature operation of microdisc lasers with submilliamp threshold current," Electronics Letters, vol. 28, no. 11, pp. 1010-1012, 1992.

[14] Yok Siang Oei, Barry Smalbrugge, Youcai Zhu, Tjibbe de Vries, Peter J. van Veldhoven, Frank W. M. van Otten, Tom J. Eijkemans, Jarosław P. Turkiewicz, Huug de Waardt, Erik Jan Geluk, Soon-Hong Kwon, Yong-Hee Lee, Richard Nötzel & Meint K. Martin T. Hill, "Lasing in metallic-coated nanocavities," Nature, vol. 1, pp. 589-594, 2007.

[15] Martin T Hill, Yok-Siang Oei, Barry Smalbrugge, Youcai Zhu, Tjibbe De Vries, Peter J Van Veldhoven, Frank WM VanOtten,Tom J Eijkemans, Jarosław P Turkiewicz, Huug De Waardt, et al. Lasing in metallic-coated nanocavities. Nature Photonics, Vol.

1, No. 10, p. 589, 2007.

[16] Gramotnev, D. K. & Bozhevolnyi, S. I. Plasmonics beyond the diffraction limit. Nat. Photonics 4, 83–91 (2010).

[17] Martin T Hill, Milan Marell, Eunice SP Leong, Barry Smalbrugge, Youcai Zhu, Minghua Sun, Peter JVan Veldhoven, Erik Jan Geluk, Fouad Karouta, Yok-Siang Oei, et al. Lasing in metal-insulator-metal sub-wavelength plasmonic waveguides. Optics express, Vol. 17, No. 13, pp. 11107–11112, 2009

[18] J. H. Lee et al., "Electrically pumped sub-wavelength metallo-dielectric pedestal pillar lasers.," Opt. Express, vol. 19, no. 22, pp. 21524–31, 2011.

[19] Kang Ding, ZC Liu, LJ Yin, MT Hill, MJH Marell, PJ Van Veldhoven, R Nöetzel, and CZ Ning. Room-temperature continuous wave lasing in deep-subwavelength metallic cavities under electrical injection. Physical Review B, Vol. 85, No. 4, p. 041301, 2012.

[20] K. Ding, M. T. Hill, Z. C. Liu, L. J. Yin, P. J. van Veldhoven, and C. Z. Ning, "Record performance of electrical injection sub-wavelength metallic-cavity semiconductor lasers at room temperature.," Opt. Express, vol. 21, no. 4, pp. 4728–33, 2013.

[21] M. K. Kim, A. M. Lakhani, and M. C. Wu, "Efficient waveguide-coupling of metal-clad nanolaser cavities," Opt. Express, vol. 19, no. 23, pp. 23504–12, 2011. [3] Ian O'Connor, Frédéric Gaffiot, "On-Chip Optical Interconnect for Low-Power," Ultra Low-Power Electronics and Design, Springer, pp. 21-39, 2004.

[22] Koh Chieda, Baifu Zhan, Takuya Okimoto, Takuo Tanemura, Yoshiaki Nakano"

Numerical Investigation on Compact Metallic-Cavity Optical Modulator Integrated on InP-Based Waveguide" International Nano-Optoelectronics Workshop , August 2015

[23] Sukmo Koo, Radwanul Hasan Siddique, and Hyuck Choo, "Quantitative analysis of a III-V tapered horn-shaped metal-clad nano-cavity as an onchip light source" AIP Advances 7, 075017 (2017)

[24] Zheng Li, and Hyuck Choo, "On-chip low-profile nano-horn metal-clad optical cavity with much improved performance" CLEO: 2014, OSA Technical Digest, (Optical Society of America, 2014),paper JTh2A.94

[25] Coldren, Larry A., Scott W. Corzine, and Milan L. Mashanovitch. Diode lasers and photonic integrated circuits. John Wiley & Sons, Vol. 218. 2012.

[26] Ankun Yang, Danqing Wang, Weijia Wang, and Teri W Odom. "Coherent light sources at the nanoscale. Annual review of physical chemistry", Vol. 68, pp. 83–99, 2017.

[27] H. Raether, "Surface Plasmons on Smooth and Rough Surfaces and on Gratings.: Springer", 1988.

[28] M.J.dams, "An-Introduction-to-Optical-Waveguides", pp.156-170, 2007

[29] Amnon Yariv, Pochi Yeh, "Photonics-Optical-Electronics-in-Modern-Communications", pp.25-30, 1982

[30] Wim Bogaerts*, Peter DeHeyn, Thomas Van Vaerenbergh, Katrien DeVos, Shankar KumarSelvaraja, Tom Claes, Pieter Dumon, Peter Bienstman, Dries VanThourhout, and Roel Baets, "Silicon microring resonators", Laser Photonics Rev.6, No. 1, 47–73 (2012)/DOI10.1002/lpor.201100017.

[31] K. S. Yee, "Numerical solution of initial boundary value problems involving Maxwell's equations in isotropic media," IEEE Trans. Antennas Propag., vol. 14, no. 3, pp. 302–307, 1966.

[32] Yi Xiao. "Research on wavelength-scale metal-clad semiconductor lasers and their waveguide coupling". PhD thesis, The Univ. of Tokyo, 2018.

[33] Sukmo Koo, Radwanul Hasan Siddique, and Hyuck Choo, "Quantitative analysis of a III-V tapered horn-shaped metal-clad nano-cavity as an on-chip light source", AIP Advances 7, 075017 (2017).

[34] R.-M. Ma, R. F. Oulton, V. J. Sorger, and X. Zhang, "Plasmon lasers: Coherent light source at molecular scales," Laser Photon. Rev. 7, 1–21 (2013).

[35] D.A.Genov, R.F.Oulton, G.Bartal,and X.Zhang, "Anomalous spectral scaling of light emission rates in low-dimensional metallic nanostructures," Phys. Rev. B 83, 245312 (2011).

[36] M.-K. Kim, A. M. Lakhani, and M. C. Wu, "Efficient waveguide-coupling of metal-clad nanolaser cavities," Opt. Express 19, 23504–23512 (2011).

[37] Yi Xiao, Richard J. E. Taylor, Chuanqing Yu, Kaiyin Feng, Takuo Tanemura, and Yoshiaki Nakano, "Room-Temperature Capsule-Shaped Wavelength-Scale Metal-Clad Laser Operating at 1550 nm", Appl. Phys. Lett. 111, 081107 (2017)

[38] Yi Xiao, Mitsuhiro Watanabe, Yuguang Wang, Takuo Tanemura, Yoshiaki Nakano, "Waveguide Coupling of Wavelength-Scale Metal-Clad Laser Diode", IEEE International Semiconductor Laser Conference 2018.

[39] Yasuo Takahashi, Kenji Yamazaki, Toru Yamaguchi, Masao Nagase, and Kenji Kurihara, Hideo Namatsu, "Three-dimensional siloxane resist for the formation of nanopatterns with minimum linewidth fluctuations," Journal of Vacuum Science & Technology B, vol. 16, no. 69, pp. 69-76, 1998.

[40] Hagen CW, Grigorescu AE, "Resists for sub-20-nm electron beam lithography with focus on HSQ state of the art," Nanotechnology, vol. 20, no. 29, p. 292001, 2009.

[41] Jean-Pierre Vilcot, Marc François, Didier Decoster, Denis Lauvernier, "Optimization of HSQ resist e-beam processing technique on GaAs material," Microelectronic Engineering, vol. 75, no. 2, pp. 177-182, 2004.

[42] Marco C. van der Krogt, Cees W. Hagen and Pieter Kruit, Anda E. Grigorescu, "Influence of the development process on ultimate resolution electron beam lithography, using ultrathin hydrogen silsesquioxane resist layers," Journal of Vacuum Science & Technology B, vol. 25, no. 6, p. 1998, 2007.

[43] Kostadin Djordjev, Sang Jun Choi, and P. Daniel Dapkus, Seung June Choi, "CH4 -based dry etching of high Q InP microdisks," Journal of Vacuum Science &

Technology B, vol. 20, p. 301, 2002.

[44] Mitsuhiro Watanabe, "Topology optimization and device fabrication of wavelength-scale metal-clad semiconductor laser".Master thesis, The Univ. of Tokyo, 2019.

[45] Zheng Li, and Hyuck Choo, "On-chip low-profile nano-horn metal-clad optical cavity   with much improved performance," CLEO:2014, 2014 OSA.

[46] Baifu Zhang, "Capsule-shaped metallic InGaAs/InP cavity laser for photonic integrated circuits −proposal, simulation and demonstration," PhD thesis, The Univ. of Tokyo, 2015.

Acknowledgements